



Ejecta Formation, Early Collisional Processes, and Dynamical Evolution after the DART Impact on Dimorphos

Fabio Ferrari¹ , Sabina D. Raducan¹ , Stefania Soldini² , and Martin Jutzi¹ 

¹Space Research and Planetary Sciences, Physics Institute, University of Bern, Bern, 3012, Switzerland

²Department of Mechanical, Materials and Aerospace Engineering, University of Liverpool, Liverpool, UK

Received 2022 March 18; revised 2022 June 21; accepted 2022 June 27; published 2022 July 28

Abstract

NASA’s DART spacecraft is planned to reach and impact asteroid Dimorphos, the small moon of binary asteroid (65803) Didymos, at a velocity of 6 km s^{-1} in late 2022 September. DART will be the first mission to test the “kinetic impactor” technique, aimed at deflecting the orbital path of a potentially hazardous asteroid. The success and effectiveness of this technique resides in the efficiency of momentum exchange between the spacecraft and the impacted target. This depends on many factors, including the cratering process, the formation of ejecta, and their fate, as they remain in the system or escape from it, carrying momentum away. Here we provide an overview of the cratering process, including ejecta formation and their subsequent dynamical evolution. We use different methodologies to model the physics of the problem, including smoothed particle hydrodynamics to model the cratering and ejecta formation process after the hypervelocity impact, N -body granular simulations to model early collisional processes between ejecta fragments right after cratering, and high-fidelity planetary propagation to model the dynamical evolution of ejecta during their purely ballistic phase. We highlight the key features of each phase and their role in defining the dynamical fate of ejecta. We investigate the effect of surface cohesion in the impacted target and identify the qualitative behavior of ejecta particles as a function of the key parameters of the problem. We provide quantitative estimates for the specific case study related to the DART–Dimorphos scenario and a selected range of target properties.

Unified Astronomy Thesaurus concepts: Asteroid dynamics (2210); Impact phenomena (779); Planetary science (1255); Astrodynamics (76); N -body problem (1082); Three-body problem (1695); Ejecta (453)

1. Introduction

NASA’s Double Asteroid Redirection Test (DART) is the first space mission designed to perform a full-scale planetary defense technology demonstration test. DART will demonstrate the effectiveness of the “kinetic impactor” technique, where a spacecraft is designed to impact at very high speed against a potentially hazardous asteroid, i.e., an object on a collision course with our planet. DART was successfully launched on 2021 November 24 and is planned to impact Dimorphos, the small moon of the nonhazardous (65803) Didymos binary asteroid system, at a relative speed of about 6 km s^{-1} . The impact is foreseen for 2022 September 26 at approximately 23:14 UTC (Rivkin et al. 2021; Fahnestock et al. 2022) and is estimated to cause a minimum 73 s change in the mutual binary orbital period, which is a measurable amount using ground-based observations. DART carries on board the Light Italian CubeSat for Imaging of Asteroid (LICIACube; Dotto et al. 2021), contributed by the Italian Space Agency. LICIACube will be deployed by DART days before the impact and will observe the outcome of the DART impact during a flyby of the Didymos system. More information on the DART impact outcome and more precise measurements of the Didymos system’s properties will be provided by ESA’s Hera spacecraft, the companion of DART in the NASA-ESA Asteroid Impact and Deflection Assessment collaboration (Michel et al. 2018). Hera will rendezvous with the Didymos system in early 2027 to

study in detail the dynamical and physical properties of the binary asteroid. Hera will also provide a precise measurement of the mass of the asteroids, which is currently largely uncertain (Naidu et al. 2020). In particular, with reference to impact-related processes, Hera will investigate the presence of fresh material on Didymos and Dimorphos, which might be ejecta reaccumulated after the DART impact. Hera will carry two CubeSats on board, Milani and Juventas, which will provide, respectively, close imaging of the DART crater (Ferrari et al. 2021a) and measurements of the internal structure of Dimorphos (Goldberg et al. 2019). In addition, Milani hosts the VISTA thermogravimeter to detect dust in the close proximity of the binary system. All of these measurements will contribute to a more precise determination of the physical processes involved during and after the DART impact, from cratering to dynamical evolution of ejected material.

The outcome of the impact test, and therefore the effectiveness of the “kinetic impactor” technique as a viable option for planetary defense, depends critically on the efficiency of momentum transfer between the DART spacecraft and Dimorphos. From a physical point of view, the overall efficiency is closely related to the impact mechanism and depends on the cratering process, including formation and ejection of excavated material. Preimpact studies estimate DART’s momentum transfer by modeling the ejecta plume using analytical models and scaling relations (e.g., Housen & Holsapple 2011; Holsapple & Housen 2012; Cheng et al. 2021; Fahnestock et al. 2022), as well as more sophisticated simulation tools, such as shock physics codes (e.g., Jutzi & Michel 2014; Raducan et al. 2019, 2022). A detailed review of the current DART impact modeling efforts is provided in Stickle et al. (2022). In addition to the impact process,

Table 1
Selected Physical and Orbital Properties of the (65803) Didymos Binary Asteroid

Description	Value $\pm 1\sigma$ Uncertainty	Source
Heliocentric Orbit		
Semimajor axis	$1.644268883 \pm 1.56e-09$ au	JPL Small Bodies Database
Eccentricity	$0.383882802 \pm 2.75e-09$	JPL Small Bodies Database
Inclination to ecliptic	$3.407768167 \pm 1.33e-06^\circ$	JPL Small Bodies Database
Longitude of ascending node	$73.22791476 \pm 9.67e-06^\circ$	JPL Small Bodies Database
Argument of perihelion	$319.233323 \pm 1.10e-05^\circ$	JPL Small Bodies Database
Orbital period	$2.108350974 \pm 5.7279e-9$ yr	JPL Small Bodies Database
Binary Orbit		
Semimajor axis	1190 ± 30 m	Naidu et al. (2020)
Eccentricity	<0.05	Naidu et al. (2020)
Orbital period	11.93 ± 0.01 hr	Naidu et al. (2020)
Physical Properties		
Equal-volume diameter of Didymos	780 ± 30 m	Naidu et al. (2020)
Equal-volume diameter of Dimorphos	164 ± 18 m	Naidu et al. (2020)
Bulk density of Didymos	2170 ± 350 kg m ⁻³	Naidu et al. (2020)
Bulk density of Dimorphos (assumed)	2170 ± 350 kg m ⁻³	Naidu et al. (2020)
Mass of the system	$5.4 \pm 0.4 \times 10^{11}$ kg	Naidu et al. (2020)

Note. The JPL Small Bodies Database can be accessed at ssd.jpl.nasa.gov.

preliminary studies have investigated the short-term dynamics of ejecta (Larson & Sarid 2021; Nakazawa et al. 2021) and their long-term evolution (Yu et al. 2017; Yu & Michel 2018). Similarly, the latter have recently been investigated in the context of the Small Carry-on Impactor experiment performed by JAXA's Hayabusa2 spacecraft on asteroid Ryugu (Soldini et al. 2020a; Villegas-Pinto et al. 2020; Wada et al. 2021). The problem of cratering and ejecta evolution is paramount to understanding the collisional processes in our solar system and also crucial to implementing effective planetary defense strategies.

The goal of this work is to provide a comprehensive overview of the whole cratering process and its main phases, from the hypervelocity impact and ejecta formation, to the short-term dynamics of ejecta as they interact through mutual collisions minutes after the impact, to their dynamical evolution. We use different methodologies to model the physics during the different phases: we use smoothed particle hydrodynamics (SPH) simulations for cratering and ejecta formation, N -body/granular dynamics simulations for the early collisional phase, and a high-fidelity astrodynamics propagator for the longer-term ejecta evolution. We reproduce DART's impact on Dimorphos from ejecta formation to their dynamical evolution, and we highlight the most important takeaways for each phase.

2. The Didymos Environment

In this section, we introduce the properties of the Didymos binary system and give an overview of its close-proximity dynamical environment. A summary of the most relevant information is reported in Table 1, including Didymos's physical properties, as well as its heliocentric and binary orbital parameters.

The dynamical environment plays a crucial role when dealing with ejecta formation and evolution. Figure 1 reports the main acceleration contributions, relevant to the dynamics of ejecta in the proximity of Didymos, as a function of the

distance from the barycenter of the Didymos system. We highlight here that Dimorphos is approximately 1% of the mass of Didymos, so the barycenter of the binary system is very close to the barycenter of the Didymos primary (approximately 10 m apart) and well within its geometrical size. These include the gravity of Didymos and Dimorphos, the third-body gravitational disturbance of the Sun, and the solar radiation pressure (SRP). To compute their gravity field, here we consider both asteroids as point-mass sources. This is a reasonable approximation for the case of the Didymos system, as the difference in acceleration fields due to a nonspherical mass distribution is minimal in the inner region of the system (on the order of a few percentage points) and completely negligible beyond the orbit of Dimorphos. A more detailed analysis of the effect of nonspherical asteroid shapes is reported in Ferrari et al. (2021b). A range of values is reported for each acceleration contribution, between an upper and lower limit, representing the minimum and maximum values registered during a full orbit of Didymos around the Sun. In particular, the accelerations due to SRP and the Sun's third-body gravity are highly dependent on the heliocentric motion of Didymos (more detail is given in Table 1) and reach a maximum at perihelion (2022 October 22) and a minimum at aphelion (2023 November 11). In this case, we consider the first perihelion and aphelion after DART's impact, which is foreseen for late 2022 September. On the other hand, the colored region between the upper and lower limits in Didymos's and Dimorphos's gravity values is not due to heliocentric motion but rather to the ~ 12 hr motion of the asteroid couple around the barycenter of the Didymos system. Figure 1 (left) reports values of acceleration due to SRP for different ejecta particle sizes, ranging from 0.1 mm to 10 cm, assuming spherical ejecta particles with a homogeneous material density of 3000 kg m⁻³. The figure shows that in such a low-gravity environment, the SRP plays a crucial role, as it is comparable to and in some cases higher than Didymos's gravity. In particular, the dynamics of centimeter-sized (or bigger) ejecta particles are

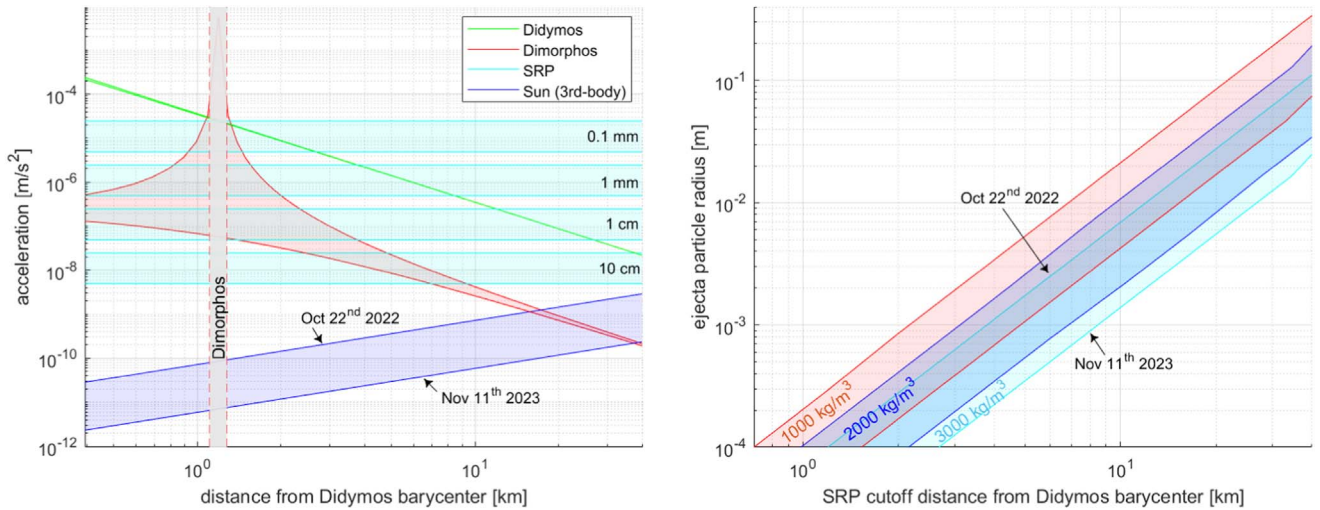


Figure 1. Acceleration environment in the close proximity of the Didymos binary system. Ranges between minimum and maximum accelerations due to the gravity of Didymos and Dimorphos (modeled as homogeneous spheres), third-body gravitational perturbation of the Sun, and SRP are shown (left). Minimum–maximum ranges are computed within a time frame between DART’s impact (2022 September 26) and 2023 December 31. These dates includes Didymos’s perihelion (2022 October 22) and aphelion (2023 November 11), which represent the limiting conditions for SRP and the Sun’s third-body perturbation. The SRP values are shown for different ejecta particle sizes, considering a homogeneous sphere with a material density of 3000 kg m^{-3} (left). The SRP cutoff distance, defined as the distance where SRP acceleration is equal to the gravity of Didymos, is shown as a function of particle size and a range of material density between 1000 and 3000 kg m^{-3} (right).

mainly driven by the gravity of Didymos in the innermost region of the binary system, i.e., within the first few kilometers from its barycenter. On the other hand, the dynamics of finer grains are mainly driven by SRP in the same region and even very close to the Didymos system. An efficient method to visualize the relative importance of dynamical effects acting on regions around the system is shown in Figure 1 (right). The SRP cutoff distance, defined as the distance where SRP acceleration is equal to Didymos’s gravity, is shown as a function of the ejecta particle radius and for three different ejecta material densities (1000 , 2000 , and 3000 kg m^{-3}). The SRP cutoff distance grows exponentially with grain size and provides a hard condition to the survivability of fine particles within the inner part of the Didymos system. For example, Figure 1 shows that for grain densities below 3000 kg m^{-3} , millimeter-sized particles are not likely to survive for a long time in the region below 4 km , as they would be blown away by SRP, which is the dominant acceleration acting on them. When dealing with medium- to long-term ejecta evolution, Figure 1 (right) provides a theoretical support to assume the size and density of ejecta particles that may survive, and therefore are worth investigating, in the innermost region of the Didymos system. This information is used in the following sections to estimate the particle size to be dynamically propagated in time.

Finally, when investigating the fate of particles ejected from Dimorphos, it is important to highlight that Didymos is a binary system, and therefore the dynamical environment in its close proximity is better modeled by a three-body problem. In this context, escape velocities from Dimorphos’s surface are on the order of ~ 4.5 (escape through L1 of the Didymos–Dimorphos system) and ~ 5.1 (escape through L2 of the Didymos–Dimorphos system) cm s^{-1} and depend on both latitude and longitude (Ferrari & Lavagna 2018). These values are considerably lower than the escape velocity for a simpler two-body problem, which is on the order of $\sim 8 \text{ cm s}^{-1}$ at Dimorphos’s equator. These values represent the limiting conditions for ejecta to leave the region of influence of Dimorphos and enter stable orbit around the Didymos system or, for even higher

velocities, escape from the system. A more detailed analysis of the energy required to leave the Didymos system is provided in Section 4, where the problem is studied in the view of the Didymos–Sun three-body system, considering a modified pseudopotential that includes the effect of SRP.

3. Methodology

In this work, we model all of the different dynamical phases involved in the DART impact event, starting from the hypervelocity impact, to early collisional processes between ejected fragments, up to their dynamical evolution in the Didymos system. We detail here the physical processes acting during each phase and assess the relevant contributions to the dynamics of ejecta. To this goal, we use different numerical tools to efficiently reproduce the physics and dynamical interactions within each phase. In particular, we define three main dynamical phases to address the evolution of ejecta.

1. *Cratering phase.* This phase starts with the DART kinetic impact on Dimorphos, as material is carved out of the newly formed, growing crater, and concludes when no more escaping ejecta are created. Due to the hypervelocity nature of the impact, this process involves extreme pressures and temperatures, making both thermodynamics and material physics paramount in the modeling process. These are resolved here by means of SPH simulations.
2. *Early collisional phase.* This phase includes the processes occurring between ejected fragments right after the cratering process and ejecta formation and before purely ballistic motion takes over. Mutual interactions between fragments involve both collision and gravitational interactions between particles and with the surrounding environment. We highlight here that not all ejecta fragments are affected by collisions to the same extent. This phase affects mostly slower and heavier ejecta, while smaller and faster ones escape right away with no or very few mutual contact interactions. In this work, the

dynamics during this phase are modeled using an N -body granular code, where ejecta are modeled as nonspherical irregular fragments.

3. *Ballistic phase.* As mutual collisions cease in the ejecta curtain, ejected fragments are subjected to the dynamical environment only. On a qualitative assessment, high-speed ejecta are the most likely to escape the system, while low-speed ones are likely to rapidly reaccrete onto Dimorphos. The rest of the ejecta are bound between these limiting conditions, and their fate depends critically on their velocity and size. We resolve the dynamics during this phase using a planetary propagator, which accurately models all of the relevant environmental effects and perturbations acting on the ejecta particles.

A more detailed methodological description is provided for each phase in the following sections. In particular, a general description of the numerical tools used is provided, highlighting the physical effects to be modeled, as well as a description of the numerical setup tuned to the specific DART/Dimorphos case study.

3.1. Cratering Phase

The complicated process of ejecta formation during cratering involves extreme pressures and temperatures, complex stress states, and mechanical effects and fracturing and requires dedicated numerical codes to understand. Here we use the Berns parallel SPH impact code (Benz & Asphaug 1995; Jutzi et al. 2008; Jutzi 2015) to resolve the effects of the DART hypervelocity impact on targets representative of asteroid Dimorphos. The Bern SPH is a shock physics code that uses a meshless particle method based on a Lagrangian formulation. The code was originally developed by Benz & Asphaug (1994, 1995) to model the collisional fragmentation of rocky bodies and was later parallelized (Nyffeler 2004) and further extended by Jutzi et al. (2008, 2013) and Jutzi (2015) to model porous and granular materials. The most recent version of the code includes a tensile fracture model (Benz & Asphaug 1994, 1995), a porosity model based on the $P - \alpha$ model (Jutzi et al. 2008, 2009), pressure-dependent strength models (Jutzi 2015), and self-gravity.

Here we model DART-like impacts on spherical and ellipsoidal asteroid targets similar to Dimorphos. For the DART impact scenario, the impact phase occurs over a relatively short period of time (up to ~ 20 minutes; see, e.g., Fahnestock et al. 2022), which represents only a small fraction of the orbit of Dimorphos. In this time frame, the ejecta remain in the region of influence of Dimorphos; therefore, for this phase, we consider only the gravity of the secondary in an inertial reference frame. In this study, we only consider vertical impacts. The exact angle of impact will depend on both the spacecraft incoming trajectory and the local slope of the target at the impact point, which may not be known prior to the impact. It is expected that any departure from a vertical impact will reduce the amount of mass and velocity ejected in the direction normal to the surface (Raducan et al. 2021). However, the direction of the total momentum vector is observed to “straighten up” as crater growth becomes more symmetric at later times, and for very large cratering efficiencies, such as the ones studied here, asymmetric ejecta is only expected at very early times (< 100 s).

Due to spatial resolution constraints, in all impact scenarios studied here, we assume a simplified geometry of the DART spacecraft. We model the projectile as a low-density ($\rho = 1000 \text{ kg m}^{-3}$) aluminum sphere, impacting the target at 6 km s^{-1} . Recent studies of the effects of the projectile geometry on the impact outcome (e.g., Owen et al. 2022; Raducan et al. 2022) found that for high cratering efficiencies like the ones studied here, the projectile geometry only affects the early, fast ejecta (Raducan et al. 2022). Models where a high-fidelity representation of the DART spacecraft was used found that a sphere impactor resulted in a larger crater than the model of the actual spacecraft (Owen et al. 2022); however, in all cases, the differences were within 10%. Both studies showed that a low-density spherical projectile is a reasonable approximation for the DART impact.

We model two target scenarios: low-resolution spherical targets and higher-resolution ellipsoidal targets. These target scenarios are described below. In both cases, the targets were simulated using the Tillotson equation of state (EoS) for basalt (Benz & Asphaug 1999) with a modified bulk modulus (Raducan & Jutzi 2022) and a pressure-dependent strength model, which asymptotes to a certain strength at high pressures (Lundborg 1967; Collins et al. 2004),

$$Y = Y_0 + \frac{fP}{1 + fP/(Y_{dm} - Y_0)}, \quad (1)$$

where P is the pressure, f is the coefficient of internal friction, Y_{dm} is the limiting strength at high pressure, and Y_0 is the cohesion. For the weak asteroid materials considered in this study, we use a constant cohesion, Y_0 , with a strain-based weakening model that prevents artificial clumping, similar to the approach used in Collins et al. (2008). Our model uses a linear relation between cohesion and total strain (ϵ_{tot}), and it is assumed that for $\epsilon_{\text{tot}} \geq 1$, cohesion is lost. The tensile strength is defined by extrapolating the yield strength (versus pressure) curve to intersect the pressure axis. Additionally, we limit the maximum negative pressure to $P_{\text{min}} \geq -Y_0$. For each target shape considered here, we simulate two target cohesions, $Y_0 = 10$ and 0 Pa.

Case 1: low-resolution spherical targets. For faster calculation times, we first investigate impacts into idealized spherical targets, modeled with lower spatial resolution. We consider the same initial setup as in Raducan & Jutzi (2022): an ~ 370 kg spherical projectile impacting a homogeneous spherical target with radius $a = 75$ m and two target cohesions, $Y_0 = 10$ and 0 Pa. In this case, the projectile mass and target radius are lower than the expected values for the DART spacecraft mass and Dimorphos radius. For both materials, the coefficient of internal friction was kept constant at $f = 0.6$, which is a good approximation for the coefficient of friction of granular materials (e.g., Hermalyn & Schultz 2014). The initial target porosity was kept constant at $\phi_0 = 40\%$ and modeled using the $P - \alpha$ model (Jutzi et al. 2008), with a simple quadratic crush curve defined by the parameters $P_s = 10$ MPa, $P_e = 0.1$ MPa, $P_t = 10$ MPa, $\alpha_t = 1$, $n_1 = 2$, and $n_2 = 2$ and initial distension, $\alpha_0 = 1.67$ (e.g., Raducan & Jutzi 2022).

To be able to numerically model the very long timescales required to see the impact effects, these SPH simulations had a limited spatial resolution of 5×10^5 SPH particles. The simulations were run until all of the SPH particles with velocities higher than 5 cm s^{-1} (approximately Dimorphos’s

L2 escape velocity; see Section 2 for further details) were ejected above the preimpact surface. This means that the SPH simulations were stopped after 500 s for the $Y_0 = 10$ Pa target and 1000 s for the $Y_0 = 0$ Pa target.

Case 2: high-resolution ellipsoidal targets. The second impact scenario considered an ~ 600 kg spherical projectile impacting an ellipsoidal target with semiaxes $a = 103.1$, $b = 79.3$, and $c = 66.1$ m, which is the current best-resolved shape of Dimorphos (Naidu et al. 2020). Compared to case 1, this setup is closer to the expected values in terms of DART spacecraft mass and the size of Dimorphos. Similar to case 1, we investigate targets with two values of cohesion, $Y_0 = 10$ or 0 Pa, and with a fixed coefficient of internal friction, $f = 0.6$. For these scenarios, the initial porosity was kept constant at 20% and modeled using a simple quadratic crush curve (Jutzi et al. 2008) defined by the parameters $P_s = 0.1$ GPa, $P_e = 0.1$ GPa, $P_t = 0.2$ GPa, $\alpha_t = 1$, $n_1 = 2$, and $n_2 = 2$ and initial distension, $\alpha_0 = 1.25$.

These models used a higher spatial resolution of 4.2×10^6 SPH particles in the target. Again, the simulations were run until all of the SPH particles with velocities higher than 5 cm s^{-1} were ejected above the preimpact surface, which was 500 s for the $Y_0 = 10$ Pa target and 1000 s for the $Y_0 = 0$ Pa target.

The relevant material parameters used in this study are summarized in Table 2. The models used self-gravity, which was recalculated every few time steps.

3.2. Early Collisional Phase

Right after impact, the newly formed cloud of ejecta undergoes a short collisional phase, where particles interact chaotically through mutual collisions. In this phase, both collision/contact interactions between fragments and the gravitational environment are important and play a role in the determination of the dynamics of ejecta before they enter the purely ballistic (no mutual physical interactions) phase. This phase is typically very short, as collisions lasts few to tens of minutes at most after the impact (Fahnestock et al. 2022). In such a short time frame, the effect of nongravitational accelerations such as SRP can be disregarded, as they do not play a significant role in the short-term dynamics of ejecta. We highlight here that not all ejecta fragments are affected by collisions to the same extent. For example, fast ejecta are made of the smaller and lighter particles that escape right away from the system with very high speeds and can be safely assumed to not take part in the early collisional phase, if not only marginally. On the other hand, slow fragments are bigger and heavier and more likely to collide with each other. For this reason, we use low-speed ejecta only to study the effects of early collisions. This choice is also consistent with the assumption we made to disregard SRP, as slow and heavy fragments are those affected the least by SRP, even in the long term. Furthermore, this is also confirmed by the outcome of simple tests we run using a cannonball SRP model (Ferrari 2019), which showed no relevant effect of SRP within this phase.

In this work, we use the GRAINS code (Ferrari et al. 2017) to model the dynamics of ejecta particles in this early collisional phase. GRAINS is a highly parallelized N -body granular code, able to resolve both contact/collision and gravitational interactions between a high number of nonspherical particles. The gravitational module of GRAINS includes a GPU-parallel implementation of the Barnes–Hut octree algorithm (Barnes &

Table 2
Material Model Parameters for Impact Simulations into Dimorphos Analogs
(Multiple Values Tested Are Separated by a Semicolon)

Description	Impactor	Spherical Target	Elliptical Target
Material	Aluminum	Basalt	Basalt
Semixis a (m)	0.54	75	103.1
Semixis b (m)	0.54	75	79.3
Semixis c (m)	0.54	75	66.1
Resolution (no. of particles)	22; 46	5×10^5	4.2×10^6
Mass (kg)	368; 605	2.86×10^{10}	4.89×10^{10}
EoS	Tillotson ^a	Tillotson ^b	Tillotson ^b
Strength model	von Mises	LUND	LUND
LUND strength parameters ^c			
Damage strength at zero pressure, Y_0 (Pa)	...	0; 10	0; 10
Strength at infinite pressure, Y_{inf} (GPa)	...	1	1
Internal friction coefficient (damaged), f	...	0.6	0.6
Porosity model parameters ($P - \alpha$) ^d			
Initial density, ρ (kg m^{-3})	1000	1600	2160
Initial porosity, ϕ_0	...	40%	20%
Initial distension, α_0	...	1.67	1.25

Notes.

^a Tillotson (1962).

^b Benz & Asphaug (1999).

^c Lundborg (1967).

^d Jutzi et al. (2008).

Hut 1986; Bartscher & Pingali 2011; Ferrari et al. 2020) and a simpler direct N^2 integrator. As the construction of the octree implies a significant overhead to the computational cost, the GPU-parallel octree is computationally very efficient for a high number of particles, typically greater than a few thousand units. For a lower N , the direct N^2 method is more convenient in terms of both computational cost and accuracy, as it does not imply any approximation to the dynamics. In this work, we mainly use the direct N^2 approach, as we deal with limited subsets of ejecta, as it will be clarified in the following, with N never exceeding a few ten thousands of particles. To represent the gravitational environment, we model both Didymos and Dimorphos as central fields. Although provisional shape models are available for both asteroids (Naidu et al. 2020), the assumption of a central field implies simplifications in second-order gravitational effects only (Ferrari & Lavagna 2018; Ferrari et al. 2021b), which have been shown not to be relevant for short-term dynamics on the order of minutes.

GRAINS is fully integrated within CHRONO (Tasora et al. 2016), a multiphysics open-source code that is widely used for granular mechanics problems. In this work, we use CHRONO capabilities to efficiently resolve contacts and collisions between nonspherical ejecta particles. In particular, we use the CHRONO:PARALLEL module, which allows a thread-based parallelization of contact interactions, enabling a substantial reduction of simulation time without any loss of accuracy. In this work, two sets of simulations are performed, each using a different method to resolve the dynamics of particles in contact.

1. *Compliant nonsmooth contacts (NSC)*. This is a constraint-based method with equations of motion formulated as a differential variational inequality and requiring the solution of a cone complementarity problem at each time step (Tasora & Anitescu 2010, 2011). Contact dynamics are modeled as impulsive collisions, and the interacting bodies exchange momentum instantaneously, according to the coefficient of restitution (CoR). The CoR is defined as the ratio between the relative velocity after and before the collision, ranging from zero (fully inelastic collision) to 1 (fully elastic collision). In this work, we used a CoR value of 0.6, which is a common assumption for gravel-like material in asteroid-related scenarios (see, e.g., Wright et al. 2022). CHRONO’s NSC has the possibility to include compliance and damping to smooth out contact interactions and reproduce the viscoelastic behavior of the material (Tasora et al. 2013). This feature comes at the cost of an increased computational burden required but contributes to greatly increase the realism of the simulation, as it overcomes the typical problem of hard-body methods of endless bouncing, where two bodies never come to a rest after they keep their mutual contact active.
2. *Smooth contact (SMC)*. This is a penalty-based method with equations of motion written as differential algebraic equations, which include a system of ordinary differential equations (i.e., the dynamics) and a set of algebraic equations (i.e., the geometrical constraints). The dynamics are modeled using a spring-dashpot system (Fleischmann et al. 2015). The collision occurs in a finite time, and its outcome depends on the values of the stiffness and damping coefficients. The SMC has been used in the past in the context of asteroid formation and evolution (Ferrari & Tanga 2020, 2022) and is very similar to the widely used soft-sphere method (Sánchez & Scheeres 2011; Schwartz et al. 2012). In this work, we use the same numerical setup used for previous works, with both normal and tangential stiffness coefficients set to $K_n = K_t = 2 \times 10^5 \text{ N m}^{-1}$, while the damping coefficients are set to $G_n = 20$ and $G_t = 40 \text{ Ns m}^{-1}$, within the range of values commonly used for granular media (Mindlin 1949; Sánchez & Scheeres 2011).

As mentioned, both approaches have been used in this work. In principle, NSC is more suitable to model fast collisions, with no or very little aggregation between fragments. On the other hand, SMC works better for slow aggregation or settling, where contact interactions are more durable in time. In our case, NSC showed better performance, as collisions within the ejecta curtain are very fast, and very low/no aggregation/sticking is observed between ejecta particles. The results presented in this work with relation to the early collisional phase refer to NSC simulations. In addition to the contact model used, it is important to highlight the role of particle shape. Previous studies demonstrated that angular shapes are crucial to reproduce realistic collision processes at low relative speeds. For example, Korycansky & Asphaug (2006, 2009) demonstrated that a significantly lower restitution coefficient is produced by off-center collisions, which are only possible between nonspherical objects. We clarify here that the term “off-center” refers to the contact geometry and not the contact trajectory; i.e., the point of contact does not lie on the line connecting the particle centers and therefore produces a torque

on the rotational motion of the individual particles. In the case of ejecta, this might translate into a relevant loss of energy for ejecta fragments, which in turn can modify their fate, and which cannot be captured with spherical particle models. In the early collisional phase, we do not consider any sticking or cohesion between fragments. In this work, cohesion is only used in the cratering phase to form ejecta; once the cohesive material is fractured, the resulting fragments are considered as individual rigid bodies.

We performed several simulations to investigate the effects of collisions right after the end of the cratering phase. The properties of each fragment are defined based on information provided by SPH simulations, as detailed in Section 3.1. In particular, the output of the SPH runs is used to provide the position, velocity, and mass for each N -body particle. This is, however, not sufficient to initialize the GRAINS simulations, where each fragment is modeled as a rigid body with six degrees of freedom (three translational, three rotational) and a nonspherical shape. The GRAINS initialization procedure, which includes the creation of ejecta particles and handoff of information from SPH simulations, is summarized as follows.

1. Particles are created at the positions provided by the SPH simulation data.
2. The particle shape is generated randomly, taking the convex envelope of a cloud of randomly generated points. This results in angular particle shapes with approximately 10 vertices and an aspect ratio (smaller-to-larger size ratio) between 0.7 and 1.
3. The size of each particle is adjusted based on the mass information available from SPH and assuming a realistic material density.
4. At this stage, a static collision check is performed to avoid physical overlaps between the newly created particle shapes. In case of geometrical overlaps, the overall size of the particles is reduced while keeping both the aspect ratio and the particle mass constant. Such volumetric reduction implies an increase of the particle’s material density. In this case, the code checks on this value not to exceed a realistic range, which in this case is set to +50% of the nominal value. Unrealistic material densities have never been observed in our simulation campaign.
5. After the geometry and location of each particle have been defined, particles’ translational velocities are initialized using the information from SPH runs. In addition, noise is added to velocity to consider a realistic scenario, as detailed in the following paragraphs.
6. Finally, the spin motion of each particle is initialized, with a uniform distribution between zero and a maximum spin value, which was determined based on impact experiments carried on-ground.

3.3. Ballistic Phase

After the collisions have ceased, the ejecta particles enter a purely ballistic phase, where the dynamics are driven by the dynamical environment of Didymos, i.e., the gravity of the asteroids, SRP, and the Sun’s and other planets’ third-body gravity. We use a subset of initial conditions provided by SPH simulations. In particular, the subset considered is

Table 3

Ejecta Cloud Data (from SPH Simulations) and Relevant Physical Parameters of the Didymos System

Description	Value
Total mass of ejecta	$5.737 \cdot 10^7$ kg
Bulk density of Didymos	2170 kg m $^{-3}$
Didymos/Dimorphos mass ratio	0.0093
Mass of Didymos	$5.278 \cdot 10^{11}$ kg

representative of the dynamical range within the ejecta cone, within a minimum and maximum velocity range, considering large fragments only. As discussed in Section 2, smaller fragments, unlike bigger and heavier ones, are highly perturbed by SRP and eventually ejected from the system. We simulate the dynamics of the ejecta during this phase using the GONEAR tool, an N -body planetary propagator written in J2000 equatorial coordinates with a reference frame centered at either asteroid Dimorphos (labeled as A_2 in the equations) or Didymos (labeled as A_1 in the equations). The GONEAR tool was developed and validated in real time for the Hayabusa2 mission (Soldini et al. 2020b, 2020c) and is here extended to the case of a binary asteroid system. The new version of the code has been fully validated for the binary asteroid case scenario using available kernels of the trajectory of Hera’s Milani cubesat (Ferrari et al. 2021b). The GONEAR tool makes use of NASA’s SPICE Toolkit package to import the ephemeris data of Didymos, Dimorphos, the solar system planets, Earth, the Moon, and the Sun. The effect of the SRP acceleration is also implemented. In this case, a simple cannonball model is used to compute the SRP acceleration (Montenbruck & Gill 2005) considering spherically shaped ejecta particles. The N -body planetary equations (note that the term N -body refers here to the inclusion of the gravitational effects of the Sun and solar system planets, not to mutual interactions between ejecta fragments, as done for the early collisional phase) are given by

$$\begin{pmatrix} \dot{X} \\ \dot{Y} \\ \dot{Z} \\ \ddot{X} \\ \ddot{Y} \\ \ddot{Z} \end{pmatrix} = \begin{pmatrix} \dot{X} \\ \dot{Y} \\ \dot{Z} \\ -\frac{\mu_{A_2}}{r^3}X + \bar{a}_{\text{Poly}_{A_2}|x} + \sum_{j=1}^{NP_j} a_{P|x_j} + a_{\text{SRP}|x} \\ -\frac{\mu_{A_2}}{r^3}Y + \bar{a}_{\text{Poly}_{A_2}|y} + \sum_{j=1}^{NP_j} a_{P|y_j} + a_{\text{SRP}|y} \\ -\frac{\mu_{A_2}}{r^3}Z + \bar{a}_{\text{Poly}_{A_2}|z} + \sum_{j=1}^{NP_j} a_{P|z_j} + a_{\text{SRP}|z} \end{pmatrix} = \begin{pmatrix} F_1 \\ F_2 \\ F_3 \\ F_4 \\ F_5 \\ F_6 \end{pmatrix}, \quad (2)$$

or, in a more compact form,

$$\dot{\mathbf{X}} = \mathbf{F}(\mathbf{X}, t), \quad (3)$$

where μ_{A_2} is the gravitational constant of Dimorphos. The first term of the right-hand side of Equation (2) (rows 4–6) represents the gravity of Dimorphos as a point mass, while the term $\bar{a}_{\text{Poly}_{A_2}}$ is the difference between the acceleration computed using Dimorphos’s polyhedron model and its point-mass representation. In particular, the polyhedron model

acceleration is expressed with respect to the asteroid body fixed rotating frame, and it is given as

$$\begin{aligned} \mathbf{a}_{\text{Poly}|_{\text{BF}}} &= -\nabla U_{\text{Poly}} \\ &= -G\sigma \left[\sum_{e \in \text{edges}} (\mathbf{E}_e \cdot \mathbf{r}_{ce}) L_e - \sum_{f \in \text{faces}} (\mathbf{F}_f \cdot \mathbf{r}_{cf}) \omega_f \right]. \end{aligned} \quad (4)$$

A rotation is required to express the polyhedron acceleration from the asteroid body fixed to the J2000 reference frame as

$$\mathbf{a}_{\text{Poly}} = \mathbf{M}_{\text{BFtoJ2000}} \cdot \mathbf{a}_{\text{Poly}|_{\text{BF}}}. \quad (5)$$

Finally, when the polyhedron model for Dimorphos is taken into account, the first term in Equation (2) is canceled out as a redundant term, resulting in $\bar{\mathbf{a}}_{\text{Poly}} = \mathbf{a}_{\text{Poly}} + \frac{\mu}{r^3} \mathbf{r}$.

The third-body acceleration for the Sun, the other planets, and Didymos as a point mass is given by

$$\mathbf{a}_{Pj} = -\mu_{Pj} \left(\frac{\Delta}{\Delta^3} + \frac{\mathbf{d}}{d^3} \right), \quad (6)$$

with $\Delta = \mathbf{r} - \mathbf{d}$, where \mathbf{r} is the spacecraft’s position vector from Dimorphos, and \mathbf{d} is the position vector of the perturbing body (P_j) from Dimorphos. When interfacing with NASA’s SPICE Toolkit, the ephemeris is often provided in a reference frame centered in the solar system barycenter (SSB). In this case, vector \mathbf{d} is given by the position vector of the planet in SSB coordinates minus the position vector of Dimorphos in SSB coordinates. The effect of the binary is thus included in the third-body acceleration term. The GONEAR tool can also handle a third-body acceleration of Didymos with a polyhedron model as

$$\mathbf{a}_{Pj} = \nabla U_{\text{poly}_{A_2}}(\Delta) + \nabla U_{\text{poly}_{A_2}}(\mathbf{d}). \quad (7)$$

Finally, GONEAR implements the SRP acceleration model of either a nondiffusive Earth-tracking flat surface or a simpler cannonball model. In this work, we only use the cannonball model to reproduce the dynamics of spherical ejecta fragments,

$$\mathbf{a}_{\text{SRP}} = C_r \frac{P_0}{c} \frac{A}{m} \left(\frac{\text{AU}}{r_{ls}} \right)^2 \frac{\mathbf{r}_{ls}}{r_{ls}}, \quad (8)$$

where \mathbf{r}_{ls} is the Sun-particle direction, A is the cross-section area, m is the particle mass, P_0 is the solar flux (1366 W m^{-2}), c is the speed of light ($2.99792458 \cdot 10^8 \text{ m s}^{-1}$), and C_r is the reflectivity coefficient of the particle.

In this paper, a preliminary analysis of the fate of the ejecta was conducted for 600 particles, considering large and low-speed ejecta fragments only, i.e., the more likely to survive the effect of SRP, as discussed in Section 2. Table 3 shows the data of all ejecta clouds and the properties given for Didymos and Dimorphos, while Table 4 shows the data derived for a single spherical particle. Both the total mass of the ejecta and the properties of individual ejecta fragments are retrieved directly from the SPH simulation output. Note that the subset of ejecta that is brought forward to subsequent phases is already filtered in size, with only the slower and heavier particles retained (see Figure 3). In this context, the mass of each “SPH particle” is retained, while the material density is assumed based on current estimates of Dimorphos’s porosity and bulk density (Naidu et al. 2020). Also, note that we use irregular shapes during the early collisional phase, and we use spheres during the ballistic phase. This is a reasonable approximation; whereas particle shape is

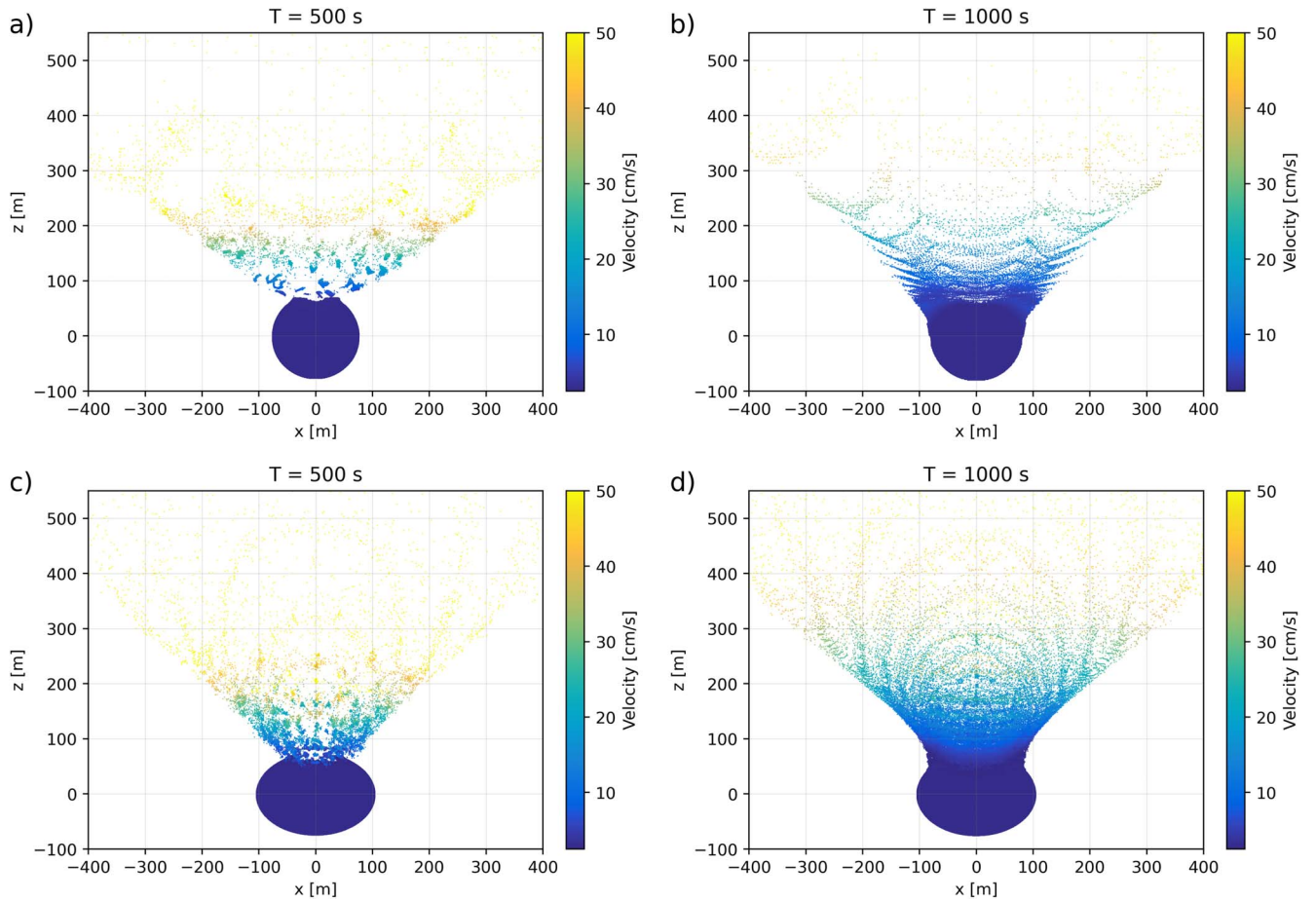


Figure 2. Profiles from Bern SPH simulations showing the target and the evolution of ejecta from impacts into (a) a spherical target with $Y_0 = 10$ Pa, (b) a spherical target with $Y_0 = 0$ Pa, (c) an elliptical target with $Y_0 = 10$ Pa, and (d) an elliptical target with $Y_0 = 0$ Pa. The profiles are plotted at (panels (a) and (c)) 500 and (panels (b) and (d)) 1000 s after the impact. The color bar shows the absolute velocity of the SPH particles.

extremely relevant to determine the outcome of interparticle collisions, this is not the case for the ballistic phase, where the shape is only used to compute the value of the cross-section surface area subject to SRP. To perform this computation, we use a spherical approximation (using the same mass and volume of irregular particles), which greatly simplifies the process without introducing any significant errors. The simulation was carried out for 1 week after DART’s impact (2022 September 26 23:15 UTC). We discuss here the results of the 1 week simulation time, as well as theoretical considerations on the long-term fate of ejecta fragments (see Section 4).

4. Results

After providing an overview of the methodology and framing the boundaries of the work’s investigations in Section 3, we report here the results of our simulation campaigns for each phase of the cratering and ejecta evolution process. In particular, data from SPH simulations are used as input in the subsequent dynamical phases to simulate the formation and evolution of ejecta from the very beginning of the cratering process.

4.1. Hypervelocity Impact and Ejecta Formation

First, we use SPH simulations to model the impact phase. From our numerical simulations, we record the mass, velocity, density, and position of each SPH particle. Figure 2 shows

Table 4
Properties of Ejecta Particles

Description	Value
Particle material density	3038 kg m^{-3} (+40% Didymos’s bulk density)
Diameter (spherical particle)	1.53 m
Area (spherical particle)	3.67 m^2
Mass (spherical particle)	5697.2 kg
C_r (reflectivity coefficient)	1.13

profiles of the SPH impact simulation outcomes using spherical (Figures 2(a) and (b)) and ellipsoidal (Figures 2(c) and (d)) targets with ($Y_0 = 10$ Pa) and without ($Y_0 = 0$ Pa) cohesion. In the case of the $Y_0 = 10$ Pa spherical target, the impact produced $\sim 3 \times 10^4 \times m$ mass of ejecta, where m is the projectile mass, out of which about $\sim 5 \times 10^3 \times m$ escapes the target gravitational field (Figure 3(a)).

Figure 3 shows the mass–velocity distribution of ejecta from our SPH simulations of impacts into spherical (Figure 3(a)) and ellipsoidal (Figure 3(b)) targets. In the case of the $Y_0 = 0$ Pa spherical target, the impact produced $\sim 4 \times 10^5 \times m$ mass of ejecta, but only $\sim 5 \times 10^3 \times m$ ejecta mass has velocities above the escape speed of Dimorphos. Similar values are obtained in the higher-resolution ellipsoidal target scenarios (Figure 3(b)). In both the spherical and ellipsoidal target scenarios, the handoff between the SPH and GRAINS simulations occurs at

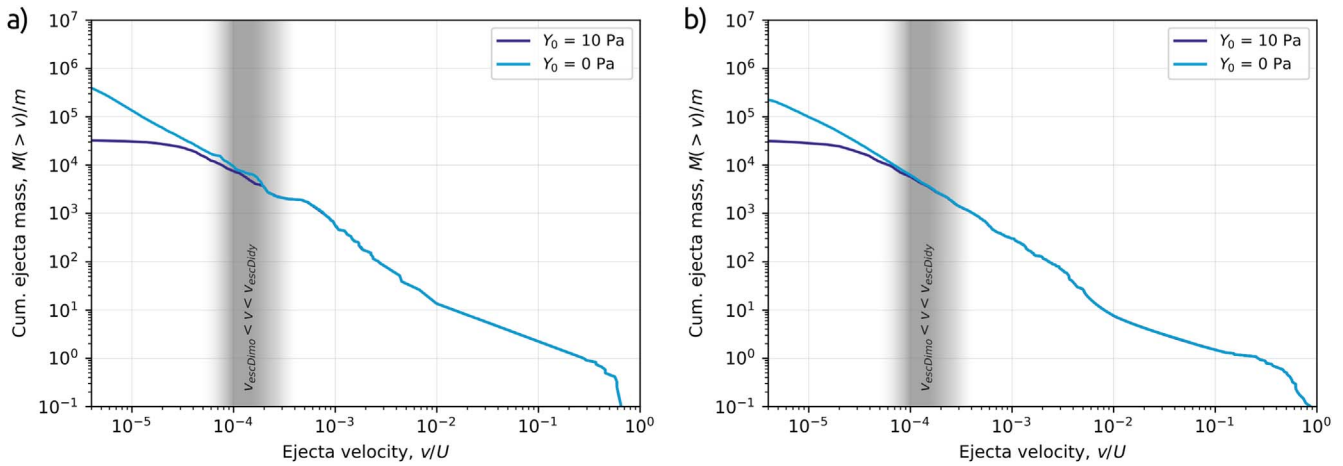


Figure 3. Normalized ejected mass (relative to the projectile’s mass) at speeds greater than v as a function of the normalized ejection speed, v/U (where U is the impact speed), for impacts into (a) spherical and (b) ellipsoidal targets with cohesions $Y_0 = 10$ and 0 Pa. The shaded area shows the velocity range between which ejected particles leave Dimorphos (higher than Dimorphos’s escape velocity) but do not escape the Didymos system (lower than the Didymos system’s escape velocity).

$T = 500$ s for the cohesive $Y_0 = 10$ Pa targets and $T = 1000$ s for the cohesionless $Y_0 = 0$ Pa targets. These handoff times correspond to the times where all of the ejected particles that are expected to leave Dimorphos (i.e., have velocities higher than the escape velocity of Dimorphos, $v > v_{\text{escDimo}}$) are above the preimpact surface level.

Due to the presence of cohesion, in the 10 Pa impact simulations, the slow material is ejected as clumps of material (Figures 2(a) and (c)). The formation mechanism and properties of these clumps are still subject to ongoing investigations; however, they may be present in nature, for instance, in the lunar ejecta (Speyerer et al. 2016; Brisset et al. 2018). In our simulations, however, these clumps may have exaggerated sizes due to resolution constraints (i.e., the clumps seem to be larger in the low-resolution simulation, Figure 2(a), compared to the high-resolution simulation, Figure 2(b)).

4.2. Short-term Ejecta Evolution

After the crater has formed and ejecta particles are produced, SPH information is handed over to GRAINS, which is used to investigate the short-term dynamics of the ejecta during the postimpact phase. All four SPH simulated cases have been studied (the low-resolution case with 0, 10 Pa and the high-resolution case with 0, 10 Pa) and used as initial conditions for GRAINS N -body simulations, as detailed in Section 3.

First of all, and for all simulation cases, we investigate the time duration of the early collisional phase. In Fahnestock et al. (2022), we reported the dependency of the duration and intensity of the collisional phase as a function of the surface density, i.e., the amount of ejecta per unit area on the ejecta cone. We extend the analysis here, providing a more detailed description of the physical phenomenon and assessing the sensitivity of collisions to the fragments’ spin rate and relative velocity. This is important, as the precise characterization of the translational and rotational velocity of each ejecta fragment is uncertain, as such motion is not resolved precisely at a particle scale in SPH simulations. To account for such uncertainty, we initialize particles with a random spin rate, and we artificially include a velocity noise in the form of a small deviation in the direction of each particle’s translational velocity. In particular, spin rates are randomly assigned to ejecta fragments according

to a uniform distribution of values between zero and a given maximum value ω_{max} . In this work, we investigate ω_{max} values within the range $0^\circ:1-3^\circ \text{ rad s}^{-1}$ (approximately $5^\circ:7-172^\circ \text{ s}^{-1}$). These values cover a very wide range of cases and are consistent with laboratory impact experiments carried out on the ground (Holsapple et al. 2002). The direction of the spin vector is also chosen randomly, with a uniform distribution covering any possible direction. The magnitude of the translational velocity is taken from SPH information for each ejecta fragment, while its direction is slightly modified to avoid unrealistic parallel trajectories of ejecta particles. In particular, we rotate the velocity vector by a random angle around a random direction in the three-dimensional space. The rotation angle is assigned according to a uniform distribution between zero and a maximum value θ_{max} . In this work, we consider θ_{max} values in the range $15^\circ-45^\circ$. We performed a simulation campaign to investigate the role of spin and translational relative velocities between ejecta fragments. We highlight that the numerical integration time step depends directly on the relative velocity between fragments. In this work, the time step is chosen to comply with the characteristic collision time, which is the fastest dynamics of the problem. In particular, spin motion produces relative speeds between fragments that linearly depend on the spin rate ω and particle radius r_{body} ($v_{\text{spin}} = \omega r_{\text{body}}$). In our simulations, the maximum admissible time step (beyond which the dynamics are too fast to be resolved) for fast-spinning fragments up to 3 rad s^{-1} is approximately 0.1 s, as relative velocities can rise up to 1.5 m s^{-1} , while it can be higher (a few seconds) for slowly spinning fragments up to 0.1 rad s^{-1} , where the relative velocities are on the order of 0.05 m s^{-1} .

In all of our simulations, we found that the early collisional phase lasts no more than 10 minutes, after which collisions among ejecta are extremely rare. Figure 4 shows a close-up of the number of collisions in time for simulations with different ω_{max} and θ_{max} for initial conditions referring to the low-resolution SPH simulation case with a 10 Pa cohesive target. We remark here that cohesion was considered only during the cratering phase while forming ejecta out of fractured surface material. Ejected fragments are individual rigid bodies, and no cohesion or sticking is considered between them. This simulates the breakup of clumps, as if they were fractured

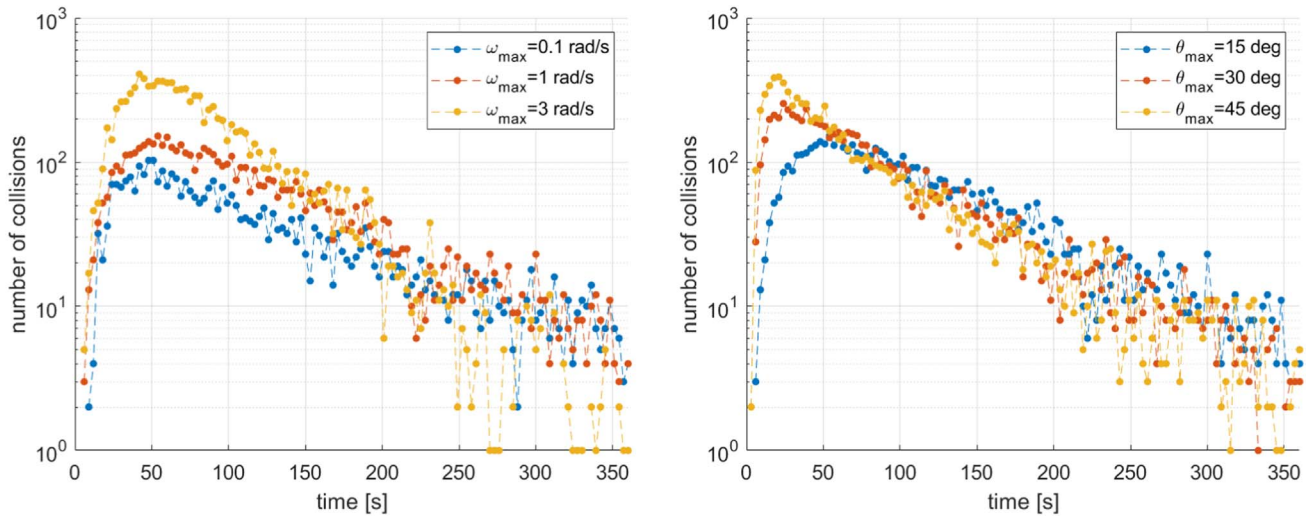


Figure 4. Number of collisions as a function of time during the early collisional phase for the low-resolution SPH simulation case with a 10 Pa cohesive target. The left panel shows the dependency on the maximum spin rate ω_{\max} of the ejecta particles. The right panel shows the dependency on the maximum deviation angle θ_{\max} , representing random noise in the direction of the translational velocity of the ejecta.

rocks where fragments break apart, no longer held together by cohesion. The results in Figure 4 are reported on a 3 s scale; i.e., each point of the curve represents the total number of collisions that occurred in the past 3 s within the ejecta cone. Some general trends can be derived. A higher spin rate of ejecta particles produces an increase in the number of collisions in the first few minutes of the simulation. In this case, compared to a lower spin rate case, particles store a higher energy due to their fast spin motion and consequently, more energy is transferred to ejecta translational motion through collisions. This, in turn, triggers more collisions to occur, involving an increased number of fragments. On the other hand, the time duration of the collisional phase is shorter for a higher particle spin rate, where a higher energy is dissipated in a shorter time frame. A similar behavior is observed when increasing the translational velocity noise. In this case, the amount of energy stored in each fragment is the same, as the noise affects the direction of velocity only, and not its magnitude. However, a higher deviation angle results in an increased number of particles intersecting their respective trajectories and therefore leading to an increased number of collisions. In addition, the peak of the collision curve is anticipated in time, and the slope after the peak has a steeper decrease for higher θ_{\max} . These results suggest that interparticle gravity is not very important during the early collisional phase, whose outcome is determined mainly by the initial dispersion of particles in both position and velocity terms.

Concerning the different initial conditions provided by SPH simulations, we observe that ejecta clumps arising from cohesive targets are more likely to trigger the collisional process between ejecta, with a higher number of collisions involved. This is consistent with the general trend shown in Fahnstoeck et al. (2022), as clumps provide regions with a higher surface density and therefore a higher likelihood of collisions. The overall effect of a cohesive target is similar to that of a higher-velocity noise, with a higher peak of collision number at the beginning of the simulation and a steeper descent of the collision curve afterward.

Overall, Figure 4 shows that the uncertainty in the spin and velocity of ejecta fragments affects the collisional processes occurring within the ejecta cone. However, the a posteriori

effect of these processes in the long-term evolution of ejecta, i.e., after the collision phase has ceased, is still uncertain. We address this problem by computing the orbital eccentricity of each ejecta particle and its evolution in time during the early collisional phase. The eccentricity is computed at each time step by considering a simple two-body problem between the ejecta fragment and the barycenter of the Didymos system,

$$\mathbf{e} = \frac{1}{\mu_D} \left(\left(v^2 - \frac{\mu_D}{r} \right) \mathbf{r} - (\mathbf{r} \cdot \mathbf{v}) \mathbf{v} \right), \quad (9)$$

$$e = \|\mathbf{e}\|, \quad (10)$$

where $\mu_D = G(M_{D_1} + M_{D_2})$ is the gravitational constant of the Didymos system, \mathbf{r} and \mathbf{v} are the position and velocity vectors of the ejecta particle with respect to the Didymos barycenter, and r and v are their norms. The eccentricity e provides a simple measure of the orbital energetic content of the ejecta particle in the Didymos system. In this context, particles with $e < 1$ are in closed orbits around Didymos and do not have enough orbital energy to escape the system, while $e > 1$ indicates that a particle is on a hyperbolic trajectory, with enough energy to escape the system. This is a simple assessment, which will be further refined in the next sections using the more realistic three-body problem framework. However, despite dynamical simplifications, the simpler two-body problem provides useful insights to quantify the effect of the early collisional phase on the dynamics of ejecta.

Figure 5 shows the number of ejecta with $e > 1$, i.e., potentially able to escape the system, during the early collisional phase. The values refer to simulations with 9160 overall ejecta fragments, considering different values of the maximum spin rate ω_{\max} and angular deviation of velocity vector θ_{\max} . To provide a direct comparison, Figure 5 shows results related to the same simulations as presented in Figure 4. All cases show a steady decrease in time of the number of particles with $e > 1$. At the initial time, approximately 6500–6650 particles have the energy to escape the system, and this number is consistently lower after 6 minutes of simulation, i.e., after most collisions have occurred. In an overall balance, we observe that a few hundred particles that

Table 5
Variations of Orbital Eccentricity and Inclination before and after the Early Collisional Phase

ω_{\max} (rad s ⁻¹)	θ_{\max} (deg)	Δe (mean \pm 3 σ) (-)	Δi (mean \pm 3 σ) (deg)	$\Delta N_{e>1}$ (-)
0.1	15	-0.06 \pm 0.15 (-2.44%)	-0.06 \pm 2.22 (-0.28%)	-242 (-3.69%)
0.1	30	-0.07 \pm 0.33 (-2.48%)	-0.10 \pm 4.99 (-0.44%)	-207 (-3.13%)
0.1	45	-0.07 \pm 0.44 (-2.61%)	-0.15 \pm 7.39 (-0.66%)	-191 (-2.89%)
1	15	-0.04 \pm 0.86 (-1.50%)	0.10 \pm 12.52 (0.49%)	-121 (-1.86%)
1	30	-0.04 \pm 0.84 (-1.70%)	0.09 \pm 12.82 (0.40%)	-132 (-2.00%)
1	45	-0.04 \pm 1.00 (-1.70%)	0.01 \pm 13.32 (0.07%)	-175 (-2.64%)

Note. Mean values and 3 σ dispersions are reported. The variation of potentially escaping particles $N_{e>1}$ is also reported. The results refer to the six simulations shown in Figure 5.

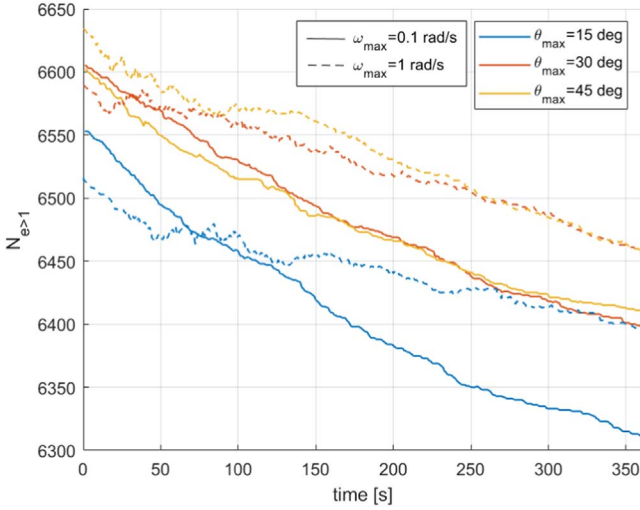


Figure 5. Number of ejecta fragments with $e > 1$ as a function of time during the early collisional phase.

would have escaped right after impact lose part of their orbital energy after the early collisional phase, ending up to eccentricity values below 1, which corresponds to bounded motion within the Didymos system. A detailed quantification of this effect is reported in Table 5, considering both the mean eccentricity value e among all ejecta particles and the number of potentially escaping particles $N_{e>1}$ and their variation before and after the early collisional phase. Results are reported for the six simulations shown in Figure 5. As mentioned, we observe a slight decrease of the mean eccentricity of the ejecta (1.50%–2.61%), which in turn produces a decrease in the number of potentially escaping particles $N_{e>1}$ on the order of a few percent (1.86%–3.69%) of all ejecta particles. In general, we observe that a higher θ_{\max} corresponds to a higher 3 σ dispersion for the value of e in the ejecta population. In the case of fast-spinning fragments, this also corresponds to a higher reduction of potentially escaping particles $N_{e>1}$, while the opposite is true for slow-spinning ejecta, where a higher θ_{\max} corresponds to a lower reduction of $N_{e>1}$. Also, we observe that cases with slow-spinning fragments have a higher dissipation of orbital energy, i.e., a higher reduction of $N_{e>1}$ compared to fast-spinning ones. This can be explained by accounting for the extra energy stored in the particles’ spin, which is transferred into kinetic translational energy, therefore increasing the orbital energy and mitigating the reduction of $N_{e>1}$. Although these $\Delta N_{e>1}$ values are relatively small, they show that collisions can contribute to lowering the overall efficiency of the impact

momentum transfer, as less ejecta escape the system and more are bound to remain within the system.

Finally, Table 5 reports the variation in the mean orbital inclination of ejecta particles Δi . Due to the symmetry of the problem, and since collisions occur at any location within the ejecta cone, we do not observe any relevant variation on the mean value of ejecta orbital inclination. On the other hand, we see that a higher-velocity noise produces a wider distribution of orbital inclinations, as its 3 σ dispersion increases with θ_{\max} . This effect is clearly visible in Figure 6, which reports the dispersion histograms referring to the cases with $\omega_{\max} = 0.1$ rad s⁻¹ (first three rows of Table 5). The same is observed for higher spin rates, where the orbital inclination distribution of ejecta is consistently wider (3 σ is higher) compared to the lower spin rate cases. We highlight here that a wider distribution of orbital inclination means a higher cone aperture angle and therefore implies important consequences for the subsequent dynamical evolution of ejecta, which are more likely to reach higher orbit inclinations. This effect is not to be confused with the typical effect played by collisions in other granular systems (e.g., planetary rings), where energy dissipation kills the out-of-plane component reducing the orbital inclination of the fragments up to a nearly planar motion. Unlike the planetary ring case, in our case (and for the short time duration of the early collisional phase), the ejecta fragments are not subject to a strong central field, which forces the particle to make repeated ring–plane crossings, and there is no sufficient surface density to increase the likelihood of collisions and trigger the “planetary ring” effect. We observe instead that increasing the number of collisions produces a more chaotic environment with a higher level of randomness in the interactions, with some particles scattered to higher-inclination orbits as a consequence.

4.3. Dynamical Evolution of Ejecta

After the collisions have ceased, the ejecta fragments enter the purely ballistic phase, and their dynamics can be safely propagated in time without considering mutual interactions between them. A preliminary analysis of the fate of ejecta is presented here. The simulation was carried out for 600 particles, starting from DART’s impact date (2022 September 26 23:15 UTC) and propagated for 1 week, until 2022 October 3 23:15 UTC. The initial conditions for this analysis have been sampled out from the ejecta cone generated after SPH simulations, considering particles not in contact with other fragments.

In particular, the following results refer to the case of an SPH cohesionless target. Among all of the ejecta fragments, 55% of

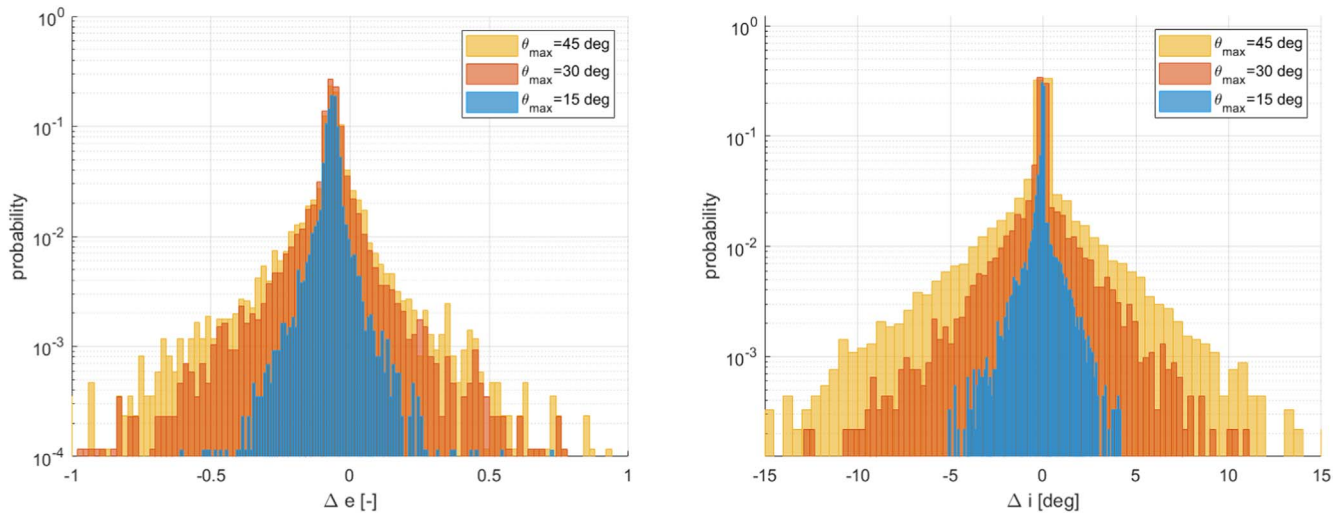


Figure 6. Dispersion of orbital eccentricity and inclination variations before and after the early collisional phase. Dispersion histograms are shown here for cases with $\omega_{\max} = 0.1 \text{ rad s}^{-1}$ reported in Table 5 (first three rows).

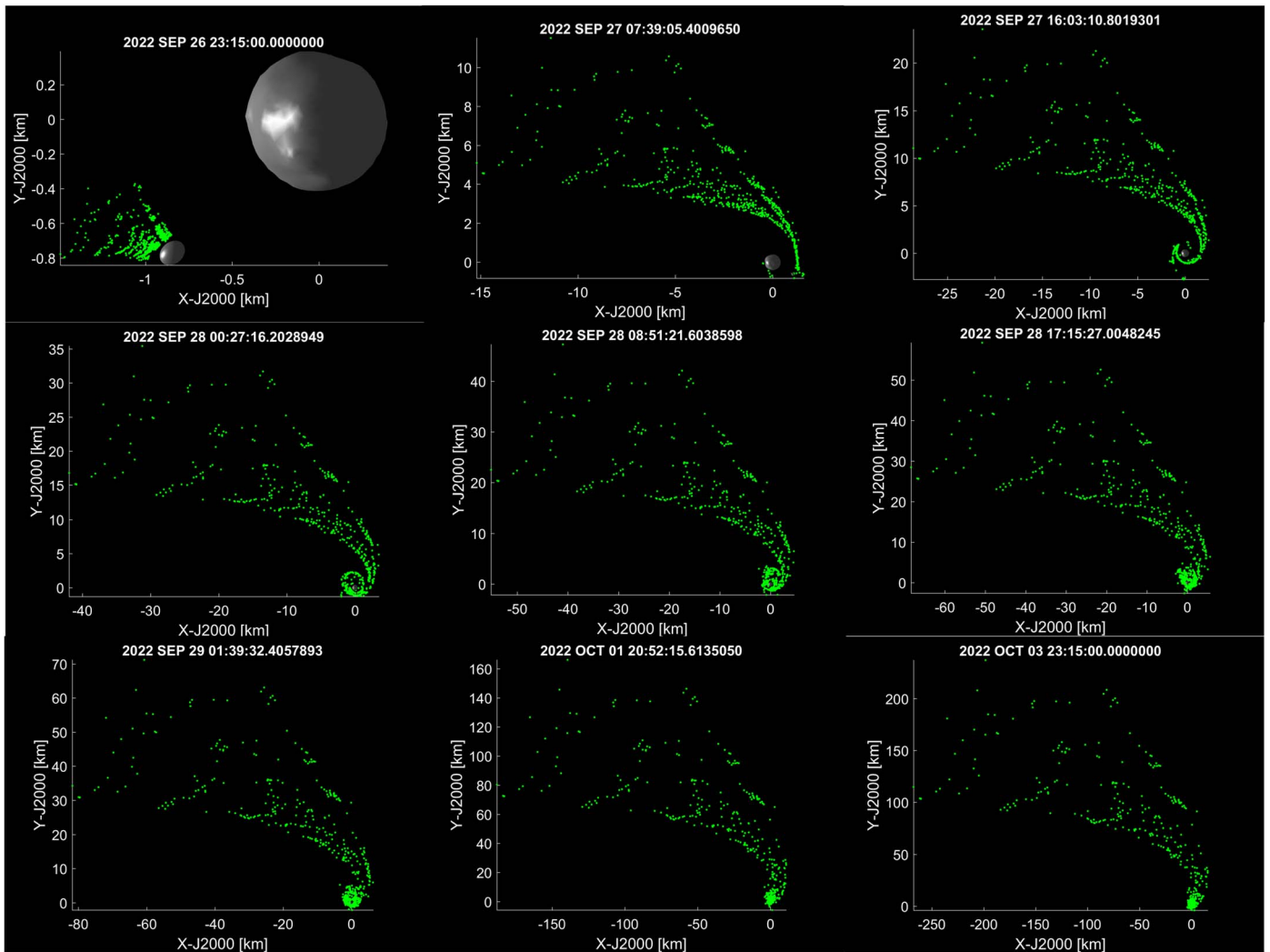


Figure 7. Fate of ejecta 1 week after DART impact.

the particles (329) are still in orbit after a week, 9% (54) have reaccumulated to Didymos, and 36% (216) have escaped the system (with a distance from Didymos above 50 km). Note that

among the solutions analyzed, there are no accretions on Didymos after 1 week. Figures 7–9 show the evolution of the ejecta particle with time from different viewing distances. In

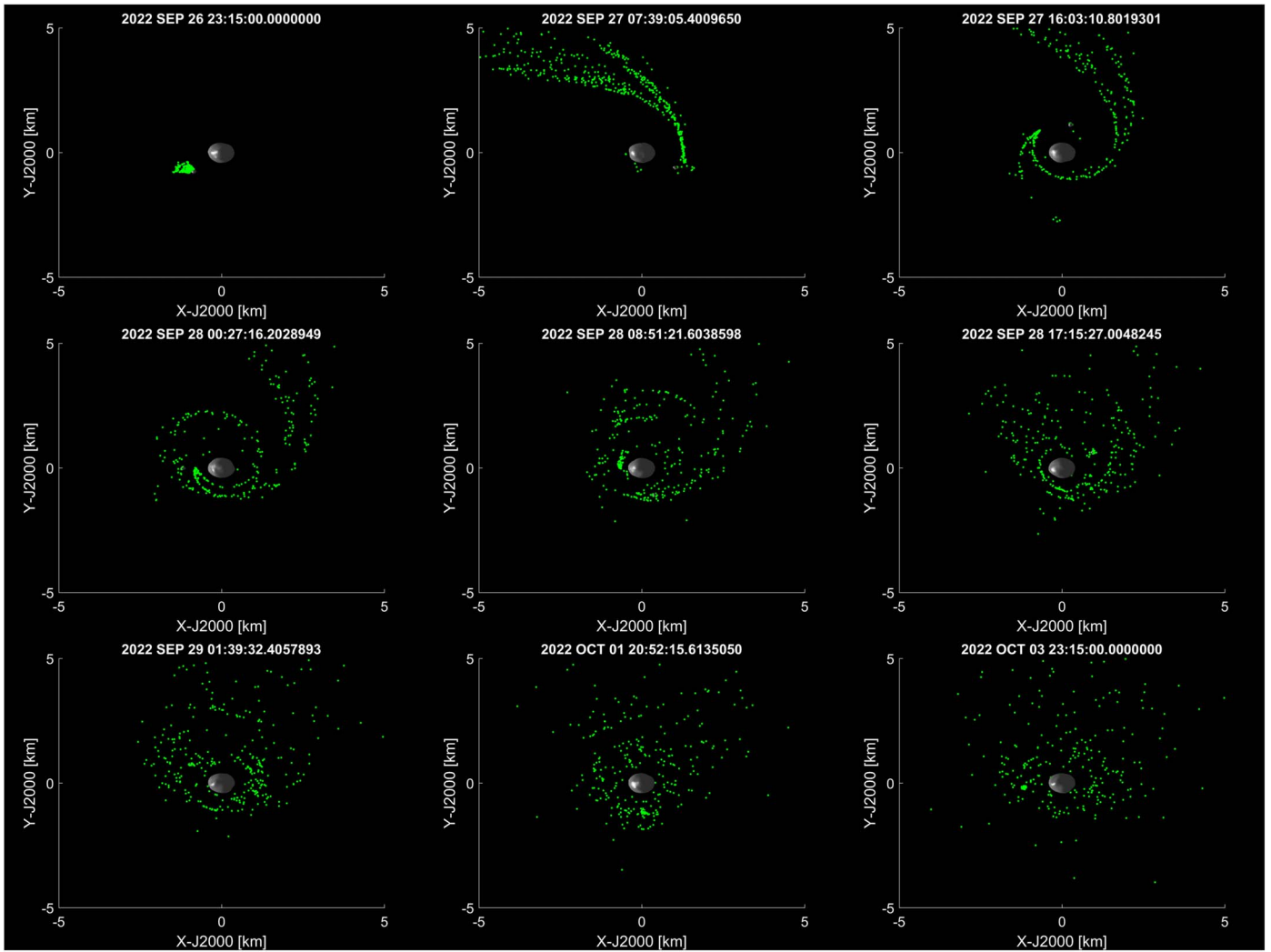


Figure 8. Fate of ejecta 1 week after DART impact; view at 5 km distance from Didymos barycenter.

particular, the views in Figures 7 and 8 suggest that most of the particles escape in the direction of Y-J2000 positive axis. This will be verified by LICIAcube, which is planned to perform observations of the ejecta plume shortly after impact. In the innermost region of the system, i.e., within a distance of 2 km from the system’s barycenter (Figure 9), ejecta particles interact closely with Dimorphos, and a few days after DART’s impact (on 2022 September 28), a trail of ejecta sharing a similar orbit with Dimorphos is observed to reimpact on Dimorphos’s surface. We remark here that these considerations apply to the specific case studied in this work, whereas results might change when considering different initial conditions (e.g., a different cone aperture angle or cone centerline direction). However, despite initial conditions that might affect the dynamics of the ejecta in the days (or weeks) following the impact, preliminary ongoing results suggest that longer-term evolution in the Didymos system is subject to chaotic motion and therefore less affected by initial conditions. This is also confirmed by works on the longer-term dynamics of DART ejecta (e.g., Rossi et al. 2022). Insights on the fate of ejecta can be retrieved from Figure 10, which compares the speed of ejecta particles at DART’s impact epoch 2022 September 26 23:15 UTC (left) with the final speed of the ejecta after a week, at 2022 October 3 23:15 UTC (right). The ejecta particles have been sorted into

three groups: reimpacting on Dimorphos (blue), orbiting the system (after 1 week; black), and escaping the system (magenta). In Figure 10, the red dashed line corresponds to Dimorphos’s two-body escape velocity (8.92 cm s^{-1}), while the black dashed line is the escape velocity from Didymos (42.3 cm s^{-1}), still under the two-body problem assumption. Note that all of the ejecta particles that reaccrete on Dimorphos within a week have an initial speed below 8.92 cm s^{-1} (Dimorphos’s escape velocity for the two-body problem), as shown in blue in Figure 10 (left). However, not all particles with a velocity below 8.92 cm s^{-1} reaccrete on Dimorphos within a week, as shown by the black curve in Figure 10. In fact, particles that remain in orbit around the system³ have speeds similar to Dimorphos’s escape velocity and in some cases above it. We also remark that some particles that reimpact Dimorphos have a speed above 8.92 cm s^{-1} , as shown for the blue solutions in Figure 10 (right); thus, the particles would have enough energy to bounce off the surface of Dimorphos again. Moreover, it is also important to highlight that escape velocities are computed at the equator on the surface of asteroids and have a specific direction in space, while most of

³ We define as “in orbit around the system” particles that tend to stay within 50 km from the center of the system.

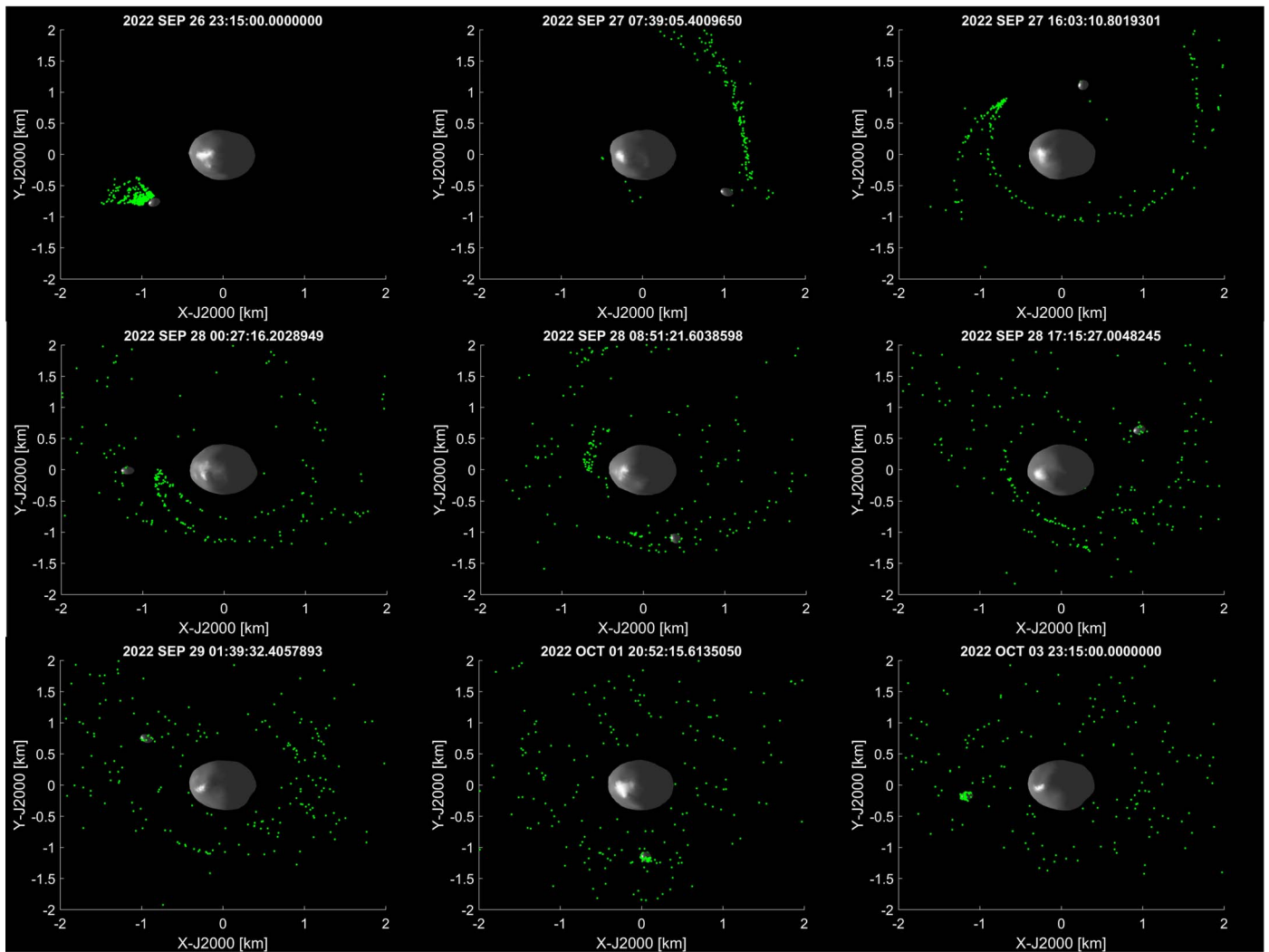


Figure 9. Fate of ejecta 1 week after DART impact; view at 2 km distance from Didymos barycenter.

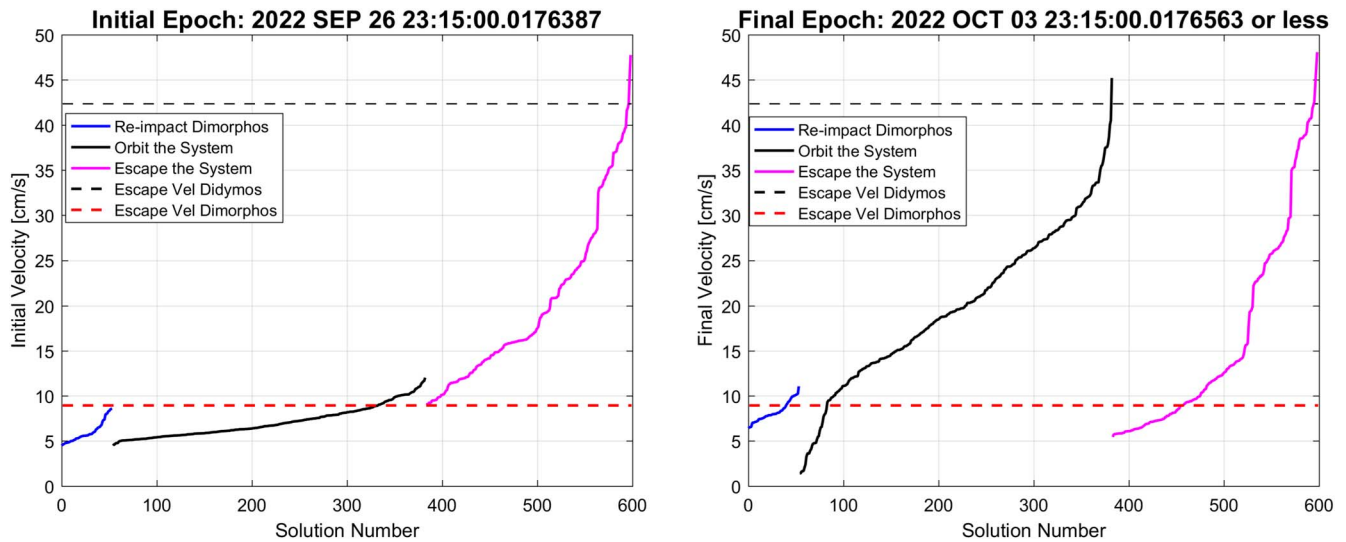


Figure 10. Comparison of the ejecta speed profile at DART’s impact (left) and a week after impact (right) for 600 solutions that reimpact Dimorphos (blue), stay in orbit around the system (black), or escape the system (magenta).

these fragments are orbiting the system, and some of them (especially among those shown in magenta) are very distant from the system and started with an initial speed above

Dimorphos’s escape velocity (left). Some escaped fragments are shown to slow down below Dimorphos’s escape velocity (right), meaning that they would leave the system slowly. This

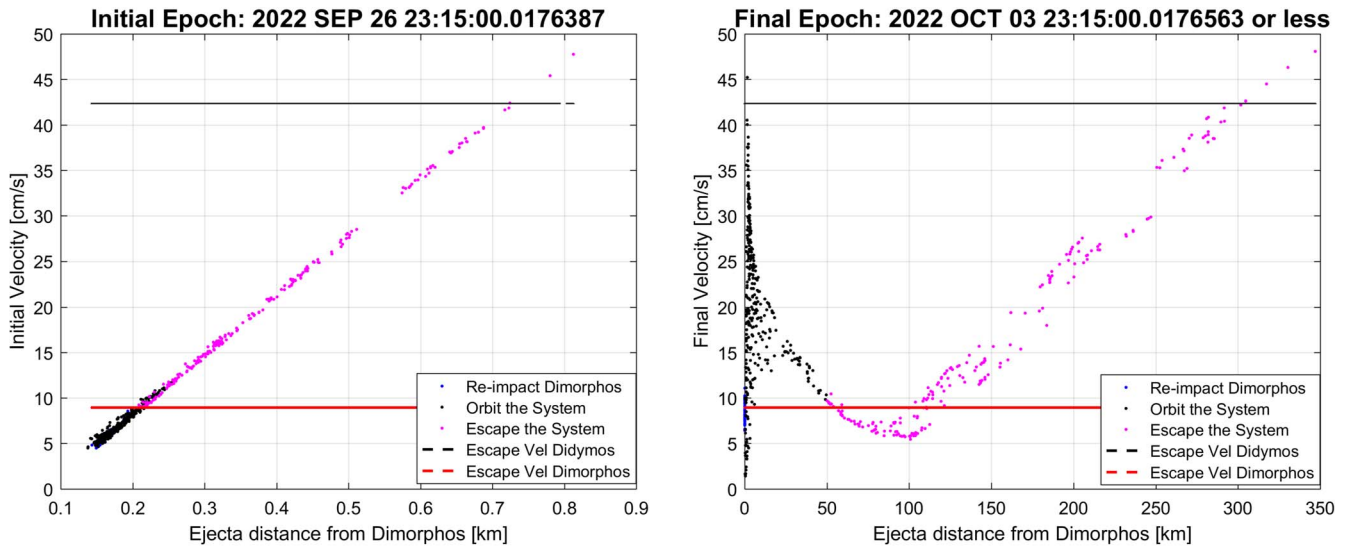


Figure 11. Comparison of the ejecta speed profile at DART’s impact (left) and a week after impact (right) as a function of their distance from Dimorphos in J2000 coordinates: reimpact Dimorphos (blue), stay in orbit around the system (black), or escape the system (magenta).

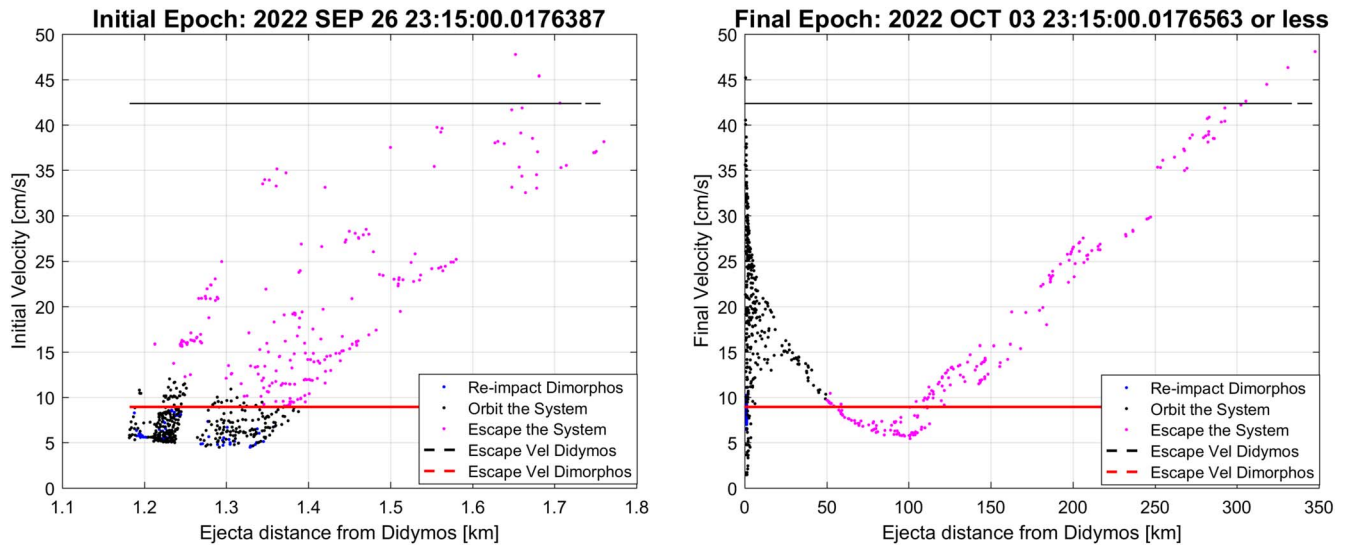


Figure 12. Comparison of the ejecta speed profile at DART’s impact (left) and a week after impact (right) as a function of their distance from Didymos in J2000 coordinates: reimpact Dimorphos (blue), stay in orbit around the system (black), or escape the system (magenta).

is also visible by looking at the speed distribution of the ejecta as a function of their distance from Dimorphos (Figure 11) or Didymos (Figure 12). Both figures are shown in J2000 coordinates.

A better interpretation of the fate of the ejecta can be provided by the orbital parameters computed for Didymos’s two-body problem. In particular, we report here the values of the eccentricity and semimajor axis, which, in the ideal two-body problem assumption, would reveal the fate of fragments remaining bound within the system ($e < 1; a > 0$) or, conversely, leaving the system ($e > 1; a < 0$). Figure 13 reports the distribution of eccentricity, semimajor axis, and inclination for the cohesive Dimorphos case (10 Pa) and shows a comparison between the initial distribution of ejecta right at the end of the cratering phase and after 24 hr. In this case, we observe a decrease of escaping ejecta (less particles with $e > 1$ and $a < 0$), as well as an increase of particles in the orbital region between Didymos and Dimorphos ($0.5 \text{ km} < a < 1.2 \text{ km}$). We

also observe a lower orbital inclination above Didymos’s binary plane for some particles. Unlike the early collisional phase, where orbital parameter variations were driven by collisions, these variations are due to the complex dynamical interactions within the Didymos three-body system. In fact, considerations of orbital parameters provide a first-order estimate of the long-term fate of ejecta but are based on a simplified model: the two-body problem. To better interpret the dynamical behavior of ejecta within a binary asteroid system, we use the more realistic circular-restricted three-body problem (CR3BP). In particular, two different three-body systems can be used to separately account for the effects of the Sun (Sun–Didymos CR3BP) and Dimorphos (Didymos–Dimorphos CR3BP).

4.3.1. The Photogravitational Hill Problem

The Hill problem of the Sun–Didymos system is investigated here for qualitative consideration of the dynamics around the

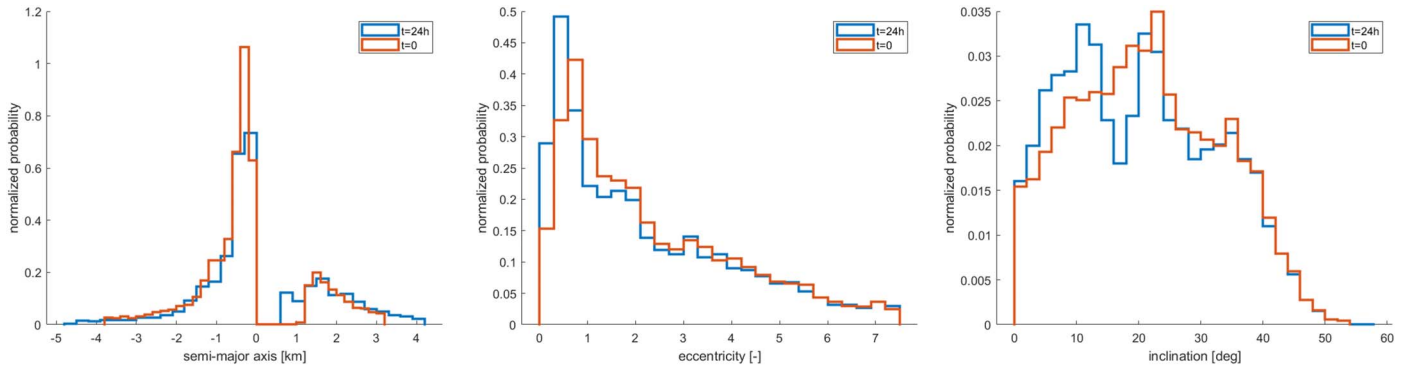


Figure 13. Distribution of orbital parameters for ejecta particles in the Didymos two-body system. Distributions are shown both at $t = 0$ (right at the end of the cratering phase) and after 24 hr.

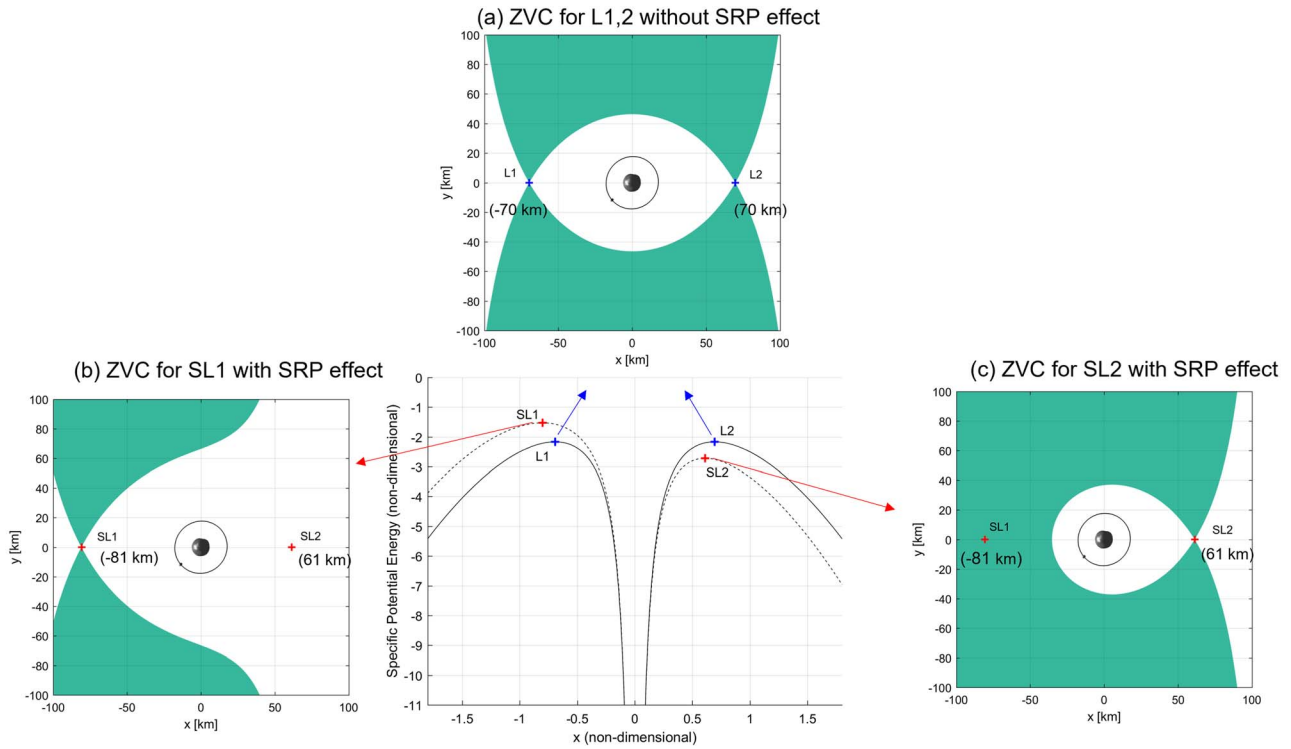


Figure 14. The ZVCs and position of L1,2 with and without the effect of SRP, shown in the Hill coordinate frame of the Sun–Didymos system. The center figure is in nondimensional coordinates. Didymos, Dimorphos, and Dimorphos’s orbit are not to scale, and Dimorphos’s position is at the epoch of impact.

Didymos system when the SRP of a spherical particle is taken into account. We focus here on the computation of the L1,2 Lagrangian points and their associated energy integral for qualitative information on the possible bounded motion of a spherical particle. The use of zero-velocity curves (ZVCs) is shown here to compare the Hill problem with the photogravitational Hill problem for an ejecta particle in the Didymos system. With reference to the synodic corotating reference frame, with x directed as the line connecting the centers of Didymos and Dimorphos, z in the binary out-of-plane components, and centered at the barycenter of the Didymos system, the energy integral is defined as

$$E = \frac{1}{2}(\dot{x}^2 + \dot{y}^2 + \dot{z}^2) - \frac{\mu_{\text{Did-sys}}}{r} - \frac{3}{2}n^2x^2 + \frac{1}{2}n^2z^2 - a_x x, \quad (11)$$

where $\mu_{\text{Did-sys}} = \mu_{\text{Didymos}} + \mu_{\text{Dimorphos}}$ is the gravitational constant of the Didymos system; n is the mean anomaly, defined as $\sqrt{\frac{\mu_{\text{Did-sys}} + \mu_{\text{Sun}}}{d^3}}$; and a_x is the SRP acceleration for a spherical particle. Here a_x is defined as

$$a_x = \frac{P_0 A}{c m} C_r \left(\frac{1 \text{ au}}{d} \right)^2, \quad (12)$$

where A and m are the area and mass of the spherical ejecta particle with values given in Table 4; P_0 is the solar flux constant (1366 W m^{-2}); c is the speed of light ($2.99792458 \cdot 10^8 \text{ m s}^{-1}$); C_r is the reflectivity property of the ejecta, here assumed as 1.13 (Table 4); and d is the distance of Didymos from the Sun at the epoch of impact (2022 September 26 23:15 UTC). The equations of equilibrium can be found by setting the velocities and accelerations of

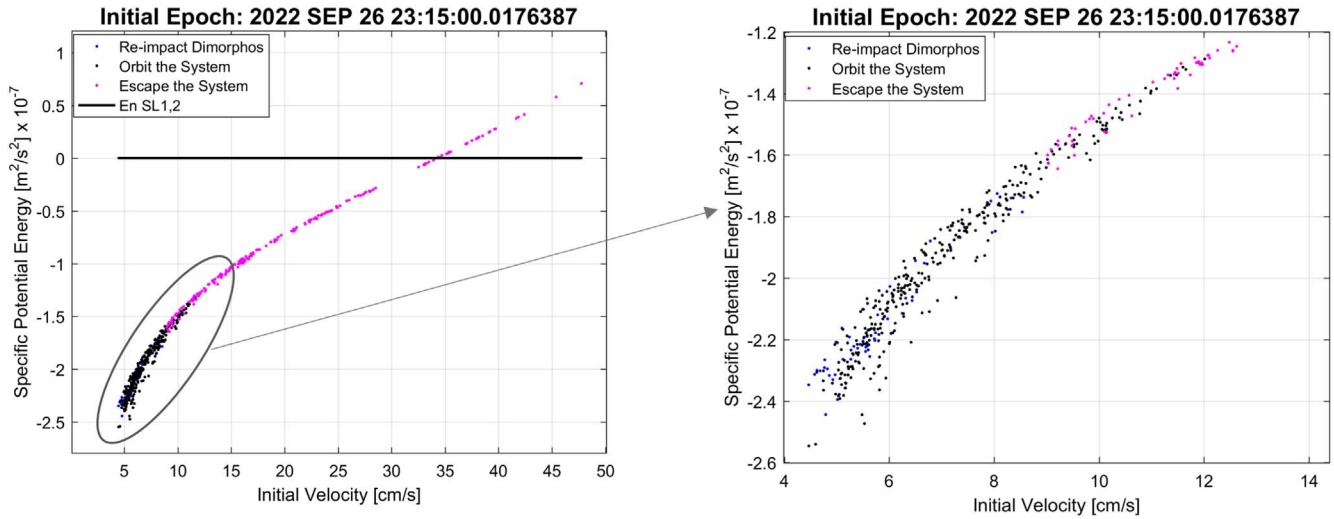


Figure 15. Specific potential energy of the ejecta particles at the time of impact in the Hill coordinate frame of the Sun–Didymos system. The right panel shows a close view of the solutions circled in gray in the left panel. Refer to Figure 10 for details on color coding.

Table 6

Specific Potential Energy, E (Equation (11)), Associated with the ZVCs in Figures 14

	E (m^2/s^2)
SL1 (data ejecta Table 4)	$-5.298219530241258\text{e-}10$
L1,2	$-7.576789883404990\text{e-}10$
SL2 (data ejecta Table 4)	$-9.558050161511058\text{e-}10$
Dimorphos	$-1.391664858517686\text{e-}08$

Equation (11) equal to zero. The coordinates of the pseudo-Lagrangian points SL1,2 are found numerically, as explained in Soldini et al. (2020c), and for an ejecta particle of properties shown in Table 4, their coordinates are $x_{\text{SL}_1} = -80.7$ and $x_{\text{SL}_2} = 61.36$ km, respectively, in the Sun–Didymos synodic reference frame, centered in Didymos. If SRP is not taken into account ($a_x = 0 \text{ m s}^{-2}$), the coordinates of L1,2 are $x_{L_{1,2}} \pm 69.72$ km. Figure 14 provides a comparison between the classic Hill problem and the photogravitational Hill problem, which includes the effect of SRP. It is interesting to note that while the potential energy of SL1 increases with respect to L1, SL2’s potential energy decreases with respect to L2. This case differs from the Sun–Earth system, where the potential energy of SL2 of the Sun–Earth system increases with respect to L2. However, in both the Sun–Earth and Sun–Didymos systems, the x -coordinates of L1,2 shift toward the Sun. This happens as the SRP acceleration has an opposite sign with respect to the Sun’s gravity, resulting in a “lower” pseudogravitational pull from the Sun. The fact that SL2 has a potential energy lower than L2 has an important implication in relation to the potential energy of the ejecta and the chances to stay in a stable orbit. Figure 14(a) shows the ZVCs for the case without SRP with potential energy for L1,2, where the green area represents a region where the motion is forbidden. Figures 14(b) and 14(c) show the ZVCs at the potential energy of SL1 and SL2, respectively. It is interesting to note that ejecta particles with energy above SL2 and below SL1 can potentially escape the system in the opposite direction from the Sun. Conversely, ejecta particles with energy below or equal to SL2 cannot

escape the Didymos system. However, a sensitivity analysis on the $K = C_r \cdot \frac{A}{m}$ parameter should be carried out to have a better understanding of the qualitative motion of the ejecta as a function of the ejecta speed and K . Table 6 lists the value of the potential energy associated with the ZVCs shown in Figure 14.

We now revise the results shown in Figure 10 with the interpretation of the Hill problem. Figure 15 shows the specific potential energy of the ejecta particle in the Sun–Dimorphos system. The color code is the same as in Figure 10. Here the x -axis corresponds to the ejecta speed at the epoch of 2022 September 26, while the y -axis shows the correspondent energy potential for the Hill problem. It is interesting to highlight that only a few particles have a specific potential energy above SL1, while most present an energy below SL2. However, if compared with Figure 16, after a week, trajectories initially labeled as escape solution (magenta) have energy above SL1, and all the solutions that reimpact Dimorphos (blue) have maintained an energy potential below SL2. This was not reflected at the start of the simulation. As shown in Figure 15, some solutions in magenta have energy below SL2, probably because at the start of the simulation, the gravitational effect of Dimorphos is dominant, and therefore the Hill problem of the Sun–Dimorphos system shows a better interpretation once the ejecta has left Dimorphos. Figure 16 shows the ZVC for two solutions of ejecta that are orbiting the system a week after impact. However, the top solution presents an energy potential above SL1, and the ejecta could either be leaving the system at low speed or potentially impact Dimorphos, considering the close approaches to Dimorphos’s surface. On the other hand, the solution below cannot escape the system because its energy potential is below SL2; thus, the particle is either bounded to the system or will reimpact Didymos or Dimorphos. It is important to notice that the effect of Dimorphos will affect the energy potential of the Sun–Didymos system, at least at the start of the simulation or when an ejecta particle has a close approach with Dimorphos. Here interpretations in the Sun–Didymos system are presented for a qualitative understanding of motion as a function of the initial ejecta speed.

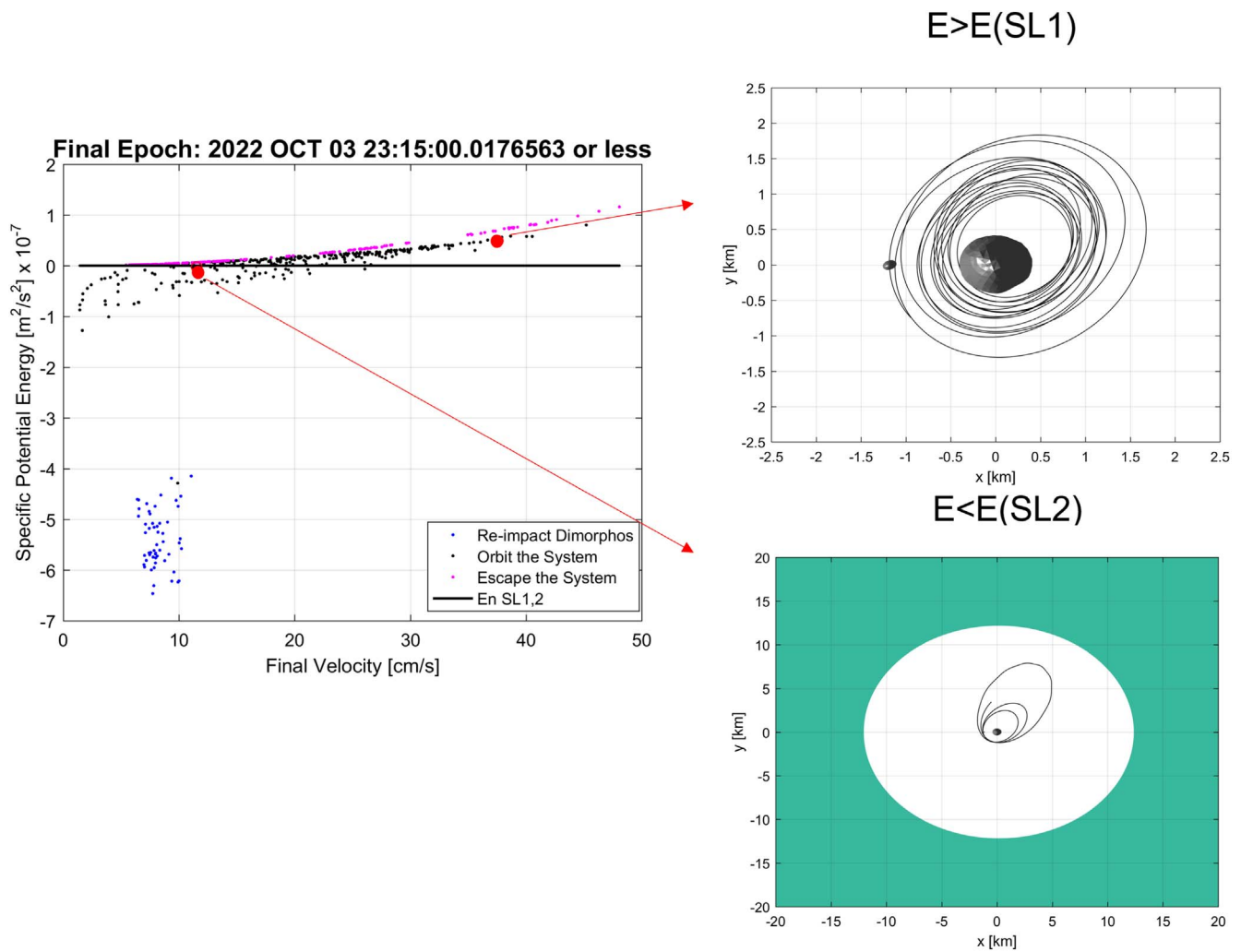


Figure 16. Specific potential energy of the ejecta particles at the time of impact in the Hill coordinate frame of the Sun–Didymos system. The trajectories on the right-hand side show the 1 week orbit of a particle, with the final specific potential energy marked in red in the left panel. Refer to Figure 10 for details on color coding.

5. Conclusion

This paper provides an overview of ejecta formation and evolution processes with specific application to the hypervelocity impact of the DART spacecraft on Dimorphos, the small moon of the Didymos binary asteroid system. We first provide an overview of the Didymos environment, highlighting regions of influence and the most dominant dynamical contributions within the system. This information is used to define the relevant dynamical effects to be reproduced during the different phases.

We study the cratering process and ejecta formation for a cohesionless Dimorphos and a surface cohesion of 10 Pa using SPH numerical simulations. We show that cohesionless targets are less likely to form clumps in the ejecta cone, while these are observed in simulations with cohesive Dimorphos targets. In general, we observe asymmetric patterns to be more likely to occur in the ejecta cone if some level of cohesion is present in the impacted soil. In this work, we investigated vertical impacts with a spherical projectile. In the context of DART impact studies, most numerical simulations assume that the projectile is an aluminum sphere, which reduces the need for resolving thin-walled structures (e.g., a spacecraft). While the DART spacecraft is significantly different from a compact sphere, the differences in resolution requirements to resolve the spacecraft structure compared to a much larger asteroid can make the simulations





extremely computationally expensive. Recent studies aimed at investigating the effects of complex projectile geometries on the mass–velocity distribution of ejecta found that for high cratering efficiencies, the projectile geometry only affects the early, fast ejecta (Raducan et al. 2022). Studies employing realistic models of the DART spacecraft found that a spherical impactor resulted in a larger crater compared to the model of the actual spacecraft (Owen et al. 2022); however, in all cases, the differences were within 10%. For what concerns the relative geometry at impact, most numerical studies of the deflection efficiency from a kinetic impactor assume that the spacecraft impacts the target at a vertical angle. However, the exact angle of impact will depend on both the spacecraft incoming trajectory and the local slope of the target at the impact point, which may not be known prior to the impact. So the impact angle adds yet another uncertainty when determining the mass–velocity of the ejecta and the momentum transfer from an impact. It is expected that a nonvertical impact will produce a reduction of the amount of mass and velocity ejected in the direction normal to the surface (Raducan et al. 2021). However, the direction of the total momentum vector is observed to “straighten up” as crater growth becomes more symmetric at later times, and for very large cratering efficiencies, such as the ones studied here, asymmetric ejecta is only expected at very early times (< 100 s).

Shortly after impact, ejecta particles undergo an early collisional phase, where they mutually interact through collisions. The early collisional phase is typically very short and lasts a few to tens of minutes. Despite its limited time duration, we observe this phase to have relevant implications on the subsequent evolution of ejecta. Collisions have the net effect of dissipating a fraction of the orbital energy possessed by the slower ejecta fragments, which are also the largest and heaviest particles excavated from Dimorphos's surface. This implies a reduction of the particles' eccentricity and semimajor axis, causing fewer fragments to escape the system. This has important consequences for the efficiency of the impact momentum exchange, which depends on momentum carried by ejecta within and outside the Didymos system. Also, a higher number of collisions is observed to initially produce a net increase in the ejecta cone angle dispersion, which in turn implies a higher dispersion in the orbital inclination of ejecta particles. This causes more ejecta to reach randomly higher orbital inclinations. We use N -body granular simulations to derive these general qualitative behaviors and quantify them for a few specific simulation cases related to the DART–Dimorphos scenario. A more comprehensive and systematic analysis is required to provide a more general quantification of collision effects on ejecta and their implications.

Finally, the dynamical evolution of ejecta is studied using accurate planetary propagation, including all dynamical effects relevant to the Didymos environment and SRP. We perform 1 week long simulations and provide a comprehensive interpretation using the theoretical framework of the photogravitational Hill problem for the Sun–Didymos three-body system. We show how this provides grounds to a more realistic prediction for the long-term fate of ejecta compared to the simpler two-body model approximation.

F.F. acknowledges funding from Swiss National Science Foundation (SNSF) Ambizione grant No. 193346. S.D.R. and M.J. have received funding from the European Union's Horizon 2020 research and innovation program under grant agreement No. 870377 (project NEO-MAPP). This work has been carried out within the framework of the National Centre for Competence in Research PlanetS supported by the Swiss National Science Foundation.

ORCID iDs

Fabio Ferrari  <https://orcid.org/0000-0001-7537-4996>
 Sabina D. Raducan  <https://orcid.org/0000-0002-7478-0148>
 Stefania Soldini  <https://orcid.org/0000-0003-3121-3845>
 Martin Jutzi  <https://orcid.org/0000-0002-1800-2974>

References

- Barnes, J., & Hut, P. 1986, *Natur*, **324**, 446
 Benz, W., & Asphaug, E. 1994, *Icar*, **107**, 98
 Benz, W., & Asphaug, E. 1995, *CoPhC*, **87**, 253
 Benz, W., & Asphaug, E. 1999, *Icar*, **142**, 5
 Brisset, J., Colwell, J., Dove, A., et al. 2018, *PEPS*, **5**, 73
 Burtscher, M., & Pingali, K. 2011, in GPU Computing Gems Emerald Edition, Applications of GPU Computing Series, ed. W.-m. W. Hwu (Boston, MA: Morgan Kaufmann), 75
 Cheng, A. F., Stickle, A. M., Fahnestock, E. G., et al. 2021, *Icar*, **352**, 113989
 Collins, G. S., Kenkmann, T., Osinski, G. R., & Wünnemann, K. 2008, *M&PS*, **43**, 1955
 Collins, G. S., Melosh, H. J., & Ivanov, B. A. 2004, *M&PS*, **39**, 217
 Dotto, E., Corte, V. D., Amoroso, M., et al. 2021, *P&SS*, **199**, 105185
 Fahnestock, E. G., Cheng, A. F., Ivanovski, S., et al. 2022, *PSJ*, in press
 Ferrari, F. 2019, in Advances in the Astronautical Sciences, ed. F. Topputo (Maui, HI: Univelt), 2065
 Ferrari, F., Franzese, V., Pugliatti, M., Giordano, C., & Topputo, F. 2021a, *AdSpR*, **67**, 2010
 Ferrari, F., Franzese, V., Pugliatti, M., Giordano, C., & Topputo, F. 2021b, *JAnSc*, **68**, 973
 Ferrari, F., & Lavagna, M. 2018, *AdSpR*, **62**, 2245
 Ferrari, F., Lavagna, M., & Blazquez, E. 2020, *MNRAS*, **492**, 749
 Ferrari, F., & Tanga, P. 2020, *Icar*, **350**, 113871
 Ferrari, F., & Tanga, P. 2022, *Icar*, **378**, 114914
 Ferrari, F., Tasora, A., Masarati, P., & Lavagna, M. 2017, *Multibody System Dynamics*, **39**, 3
 Fleischmann, J., Serban, R., Negrut, D., & Jayakumar, P. 2015, *Journal of Computational and Nonlinear Dynamics*, **11**, 044502
 Goldberg, H. R., Karatekin, O., Ritter, B., et al. 2019, Small Satellites Conf. (Logan, UT: Small Sat), <https://digitalcommons.usu.edu/smallsat/2019/all2019/73/>
 Hermalyn, B., & Schultz, P. H. 2014, *LPSC*, **45**, 2791
 Holsapple, K., Giblin, I., Housen, K., Nakamura, A., & Ryan, E. 2002, in Asteroids III, ed. W. F. Bottke, Jr. et al. (Tucson, AZ: Univ. Arizona Press), 443
 Holsapple, K. A., & Housen, K. R. 2012, *Icar*, **221**, 875
 Housen, K. R., & Holsapple, K. A. 2011, *Icar*, **211**, 856
 Jutzi, M. 2015, *P&SS*, **107**, 3
 Jutzi, M., Benz, W., & Michel, P. 2008, *Icar*, **198**, 242
 Jutzi, M., & Michel, P. 2014, *Icar*, **229**, 247
 Jutzi, M., Michel, P., Hiraoka, K., Nakamura, A. M., & Benz, W. 2009, *Icar*, **201**, 802
 Jutzi, M., Thomas, N., Benz, W., et al. 2013, *Icar*, **226**, 89
 Korycansky, D., & Asphaug, E. 2006, *Icar*, **181**, 605
 Korycansky, D., & Asphaug, E. 2009, *Icar*, **204**, 316
 Larson, J. N., & Sarid, G. 2021, *MNRAS*, **503**, 1070
 Lundborg, N. 1967, *International Journal of Rock Mechanics and Mining Sciences & Geomechanics Abstracts*, **4**, 269
 Michel, P., Kueppers, M., Sierks, H., et al. 2018, *AdSpR*, **62**, 2261
 Mindlin, R. 1949, *JAM*, **16**, 259
 Montenbruck, O., & Gill, E. 2005, *Satellite Orbits Model, Methods and Applications* (Berlin: Springer)
 Naidu, S., Benner, L., Brozovic, M., et al. 2020, *Icar*, **348**, 113777
 Nakazawa, K., Okuzumi, S., Kurosawa, K., & Hasegawa, S. 2021, *PSJ*, **2**, 237
 Nyffeler, B. 2004, PhD thesis, Univ. Bern
 Owen, J. M., DeCoster, M. E., Graninger, D. M., & Raducan, S. D. 2022, *PSJ*, submitted
 Raducan, S. D., Davison, T. M., & Collins, G. S. 2021, *Icar*, **374**, 114793
 Raducan, S. D., Davison, T. M., Luther, R., & Collins, G. S. 2019, *Icar*, **329**, 282
 Raducan, S. D., & Jutzi, M. 2022, *PSJ*, **3**, 128
 Raducan, S. D., Jutzi, M., Davison, T. M., et al. 2022, *IJIE*, **162**, 104147
 Rivkin, A. S., Chabot, N. L., Stickle, A. M., et al. 2021, *PSJ*, **2**, 173
 Rossi, A., Marzari, F., Brucato, J. R., et al. 2022, *PSJ*, **3**, 118
 Sánchez, P., & Scheeres, D. J. 2011, *ApJ*, **727**, 120
 Schwartz, S. R., Richardson, D. C., & Michel, P. 2012, *Granular Matter*, **14**, 363
 Soldini, S., Takanao, S., Ikeda, H., et al. 2020a, *P&SS*, **180**, 104740
 Soldini, S., Takeuchi, H., Taniguchi, S., et al. 2020b, *AsDyn*, **4**, 265
 Soldini, S., Yamaguchi, T., Tsuda, Y., Saiki, T., & Nakazawa, S. 2020c, *SSRv*, **216**, 108
 Speyerer, E. J., Povilaitis, R. Z., Robinson, M. S., Thomas, P. C., & Wagner, R. V. 2016, *Natur*, **538**, 215
 Stickle, A. M., Burger, C., Caldwell, W. K., et al. 2022, *PSJ*, submitted
 Tasora, A., & Anitescu, M. 2010, *Journal of Computational and Nonlinear Dynamics*, **5**, 031004
 Tasora, A., & Anitescu, M. 2011, *CMAME*, **200**, 439
 Tasora, A., Anitescu, M., Negrini, S., & Negrut, D. 2013, *International Journal of Non-Linear Mechanics*, **53**, 2
 Tasora, A., Serban, R., Mazhar, H., et al. 2016, in High Performance Computing in Science and Engineering, ed. T. Kozubek (Cham: Springer), 19
 Tillotson, H. J. 1962, General Atomic Report *GA-3216*, 141
 Villegas-Pinto, D., Soldini, S., Tsuda, Y., & Heiligers, J. 2020, in AIAA Scitech 2020 Forum (Reston, VA: AIAA), <https://arc.aiaa.org/doi/10.2514/6.2020-0221>
 Wada, K., Ishibashi, K., Kimura, H., et al. 2021, *A&A*, **647**, A43
 Wright, E., Quillen, A. C., Sánchez, P., et al. 2022, *Icar*, **376**, 114868
 Yu, Y., & Michel, P. 2018, *Icar*, **312**, 128
 Yu, Y., Michel, P., Schwartz, S. R., Naidu, S. P., & Benner, L. A. 2017, *Icar*, **282**, 313